JOURNAL OF GEOPHYSICAL RESEARCH, VOL. 105, NO. B10, PAGES 23,537–23,555, OCTOBER 10, 2000

Three-dimensional seismic structure and physical properties of the crust and shallow mantle beneath the East Pacific Rise at 9°30'N

Robert A. Dunn[1] and Douglas R. Toomey

Department of Geological Sciences, University of Oregon, Eugene

Sean C. Solomon

Department of Terrestrial Magnetism, Carnegie Institution of Washington, Washington, D.C.

Abstract. The seismic structure of the crust and shallow mantle beneath the East Pacific Rise near 9°30'N is imaged by inverting *P* wave travel time data. Our tomographic results constrain for the first time the three-dimensional structure of the lower crust in this region and allow us to compare it to shallow crustal and mantle structure. The seismic structure is characterized by a low-velocity volume (LVV) that extends from 1.2 km depth below the seafloor into the mantle. The cross-axis width of the LVV is narrow in the crust (5-7 km) and broad in the mantle (~18 km). Although the width of the top of the LVV is similar to previous estimates, its narrow shape at lower crustal depths and its significant widening in the mantle are previously unknown features of the rise velocity structure. In the rise-parallel direction the LVV varies in magnitude such that the lowest velocities are located between two minor rise axis discontinuities near 9°28'N and 9°35'N. From the seismic results we estimate the thermal structure and melt distribution beneath the rise. The thermal structure suggests that heat removal is relatively efficient throughout the crust yet inefficient at Moho and mantle depths. Estimates of the melt distribution indicate that magma accumulates at two levels in the magmatic system. One is at the top of the magmatic system and is capped by the shallow melt lens detected by seismic reflection surveys; the other is within the Moho transition zone and topmost portion of the mantle. The highest melt fractions occur within the upper reservoir, whereas the lower reservoir contains a lower melt fraction distributed over a broader area. By volume, however, there may be up to 40% more melt in the lower reservoir than in the upper reservoir. Along-axis variations in crustal melt content are similar to those in the mantle, supporting the hypothesis that the mantle, midway between the 9°28'N and 9°35'N devals, is presently delivering greater amounts of melt to the lower crust than to regions immediately to the north or south. We see no evidence (from seismic anisotropy) for diapiric mantle flow, suggesting that solid-state flow and melt migration are decoupled in the shallow mantle. Our results are not compatible with models that require a large, segment-scale redistribution of melt within the crust. Instead, our results imply that crustal magma chambers are replenished at closely spaced intervals along the rise.

1. Introduction

Our knowledge of the distribution of magma beneath active ridges derives mainly from seismic experiments. In particular, past studies of the East Pacific Rise (EPR) have determined the structure of shallow to midcrustal magma reservoirs beneath fast spreading ridges (see reviews by *Sinton and Detrick* [1992] and *Solomon and Toomey* [1992]). Still poorly understood, however, is the physical structure of the magmatic system within the lowermost crust and uppermost mantle. Consequently, the manner in which melt is delivered from the mantle to the crust and the presence or storage of melt at shallow mantle to lower crustal depths are still at issue.

Many previous studies of the EPR have indicated that melt accumulates predominantly at the top of the magmatic system within, and immediately below, a shallow crustal melt lens [e.g., *Detrick et al.*, 1987; *Mutter et al.*, 1988; *Kent et al.*, 1993]. The crustal melt lens, which is narrow and thin (about 1 km wide and 10 to 50 m thick [e.g., *Kent et al.*, 1993]), caps a broader, partially molten region characterized by low seismic velocities [*Harding et al.*, 1989; *Toomey et al.*, 1990; *Vera et al.*, 1990; *Caress et al.*, 1992] and high attenuation [*Wilcock et al.*, 1992, 1995]. From seismic velocity and seafloor compliance studies it is now known that magma accumulates within or beneath the crust-mantle transition zone or Moho [*Garmany*, 1989; *Dunn and Toomey*, 1997; *Crawford et al.*, 1999]. Such accumulations of magma occur as melt-filled sills [*Garmany*, 1989; *Crawford et al.*, 1999] and as larger volumes of partially molten material [*Dunn and Toomey*, 1997]. These broad generalizations, however, leave open such issues as the volume of the lower crust that is

[1]Now at Department of Geological Sciences, Brown University, Providence, Rhode Island.

Paper number 2000JB900210.
0148-0227/00/2000JB900210$09.00

partially molten, the shape of this region, and the fraction of melt that is present at any given depth.

Mapping the cross-axis physical structure of the region connecting mantle and crustal magma reservoirs may help us to understand how melt accumulating at subcrustal depths is transported to the crust and thus to narrow the range of acceptable models of crustal emplacement. On the basis of previous seismic results and studies of ophiolites, two classes of crustal emplacement models have been proposed. In one view, all crustal material, including the lowermost crust, passes through the shallow crustal melt lens prior to solidification [*Henstock et al.*, 1993; *Phipps Morgan and Chen*, 1993; *Quick and Denlinger*, 1993]. The lower crust in this model is formed by transporting crystallized material downward from the base of the melt lens. The contrasting view holds that the lowermost crust forms entirely in situ by repeated injection of sills that tap melt from the shallow mantle [*Boudier et al.*, 1996; *Kelemen et al.*, 1997]. In the latter model, up to 50% of the mass of lower crustal sills crystallizes to form a sequence of layered gabbros, while the remaining melt moves upward to the shallow melt lens. These models, which differ in how the fraction of melt varies at middle to lower crustal depths, may be distinguished by determining the physical structure of this region.

Knowledge of the along-axis variation in physical structure will also help us to understand the origin of rise-parallel variations in volcanic, hydrothermal, and morphologic features. Along the EPR, the seafloor depth varies, with the deepest portions near tectonic offsets, such as fracture zones and overlapping spreading centers (OSCs) [e.g., *Macdonald*, 1989]. Between these offsets, the EPR is segmented by minor morphologic deviations from axial linearity (or devals [*Langmuir et al.*, 1986]) at intervals of 5 to 25 km. Individual deval-bounded segments are thought to be associated with separate hydrothermal and shallow volcanic systems [*Haymon et al.*, 1991], petrologically distinct lavas [*Langmuir et al.*, 1986], short-wavelength variations in axial gravity and magnetization anomalies [*Lee*, 1995; *Lee et al.*, 1996], and the segmentation of crustal and upper mantle seismic velocity structure [*Toomey et al.*, 1990, 1994; *Dunn and Toomey*, 1997]. In some instances, a seismic reflector, which defines the shallow crustal melt lens, also changes in character near devals [*Kent et al.*, 1993]. These observations have been used to support differing models of magma supply to the ridge. In one extreme, magma injection from the mantle to the crust occurs at widely spaced intervals (many tens of kilometers) [e.g., *Francheteau and Ballard*, 1983; *Whitehead et al.*, 1984; *Macdonald*, 1989; *Batiza and Niu*, 1992], perhaps from melt-rich mantle diapirs [*Nicolas and Rabinowicz*, 1984; *Rabinowicz et al.*, 1984, 1987; *Barth and Mutter*, 1996; *Nicolas et al.*, 1996; *Wang et al.*, 1996], and includes along-axis redistribution of magma within the crust. Another class of model predicts that magma is supplied from the mantle to the crust at intervals comparable to the deval-related segmentation [e.g., *Langmuir et al.*, 1986; *Toomey et al.*, 1990; *Dunn and Toomey*, 1997]. Mapping the distribution of melt at mantle and crustal depths should distinguish between such models.

In this paper we present tomographic images of both isotropic and anisotropic compressional wave velocities from the seafloor to the uppermost mantle beneath the EPR at 9°30'N. Isotropic velocities are primarily sensitive to temperature and the presence of melt, whereas seismic anisotropy is sensitive to flow-induced alignment of anisotropic minerals and some distributions of melt. We emphasize results related to (1) the shape and magnitude of the subaxial low-velocity volume and its implications for the thermal structure and the storage of melt beneath the rise, (2) the along-axis variation of the low-velocity volume and its implications for the manner in which mantle-derived melt is delivered to the rise, and (3) the nature of seismic anisotropy, its implications for the pattern of mantle flow, and its correlation with the inferred melt delivery system.

2. Experiment Layout and Data

The seismic data were collected in 1988 along the East Pacific Rise (EPR) at 9°30'N, midway along a 100-km-long section of the EPR bounded by the 9°03'N OSC and the Clipperton transform (Figure 1a). The axial extent of our experiment (31 km) included a 13-km-long linear rise segment, bounded by devals near 9°28'N and 9°35'N (Figure 1b) and portions of adjacent segments to the north and south. The objective of the seismic tomography experiment was to determine the seismic structure of the crustal magmatic system [*Toomey et al.*, 1990]. The data have been used to constrain *P* wave velocity structure in the middle to uppercrust [*Toomey et al.*, 1990, 1994], crustal attenuation structure [*Wilcock et al.*, 1992, 1995], and mantle velocity and anisotropy structure [*Dunn and Toomey*, 1997]. Until now, the data have not been used to image lower crustal velocity structure, in part because seismic energy propagation in the vicinity of the magmatic system is complex [*Wilcock et al.*, 1993] and tomographic techniques, until recently [*Toomey et al.*, 1994], could not accurately and efficiently model diffracted or secondary arrivals.

During the experiment an array of 15 ocean bottom seismographs recorded compressional waves generated by 480 near-surface explosive shots (Figure 1). Detailed descriptions of the instruments, the shots, and their locations and uncertainties are given by *Toomey et al.* [1994] and *Wilcock et al.* [1995]. From the results of finite difference modeling of seismic energy propagation through a structure similar to the EPR [*Wilcock et al.*, 1993], we identified and measured arrival times of primary and secondary phases that were not previously included in a tomographic analysis. Figure 2 illustrates the ray paths and shows examples of waveforms of compressional phases that we identified. Depending on the relative position of a source and receiver with respect to the rise axis, different compressional phases were recorded, as shown in the record sections of Figure 3. In addition to a primary crustal (*Pg*) and mantle (*Pn*) refraction, *Wilcock et al.* [1993] modeled a diffraction above the shallow axial melt lens (*dPa*) and two secondary arrivals that sample the middle to lower crust beneath the rise. One of the secondary arrivals turns within ~2 km of the bottom of the shallow melt lens (*dPb*), while the other is a Moho-turning phase (*PmP*). Depending on source and receiver geometry, *PmP* arrivals were recorded for paths that did and did not cross the rise axis, as well as for paths that traveled along the rise axis. *PmP* wave paths in our data set cross the rise axis at a variety of depths, from about 4 km below the seafloor to the Moho. For rise-crossing paths, *Pn* arrivals were recorded on all off-axis instruments at ranges >32 km.

Our tomographic analysis includes travel times from 3080 primary crustal arrivals (*Pg*), 822 diffractions above the melt

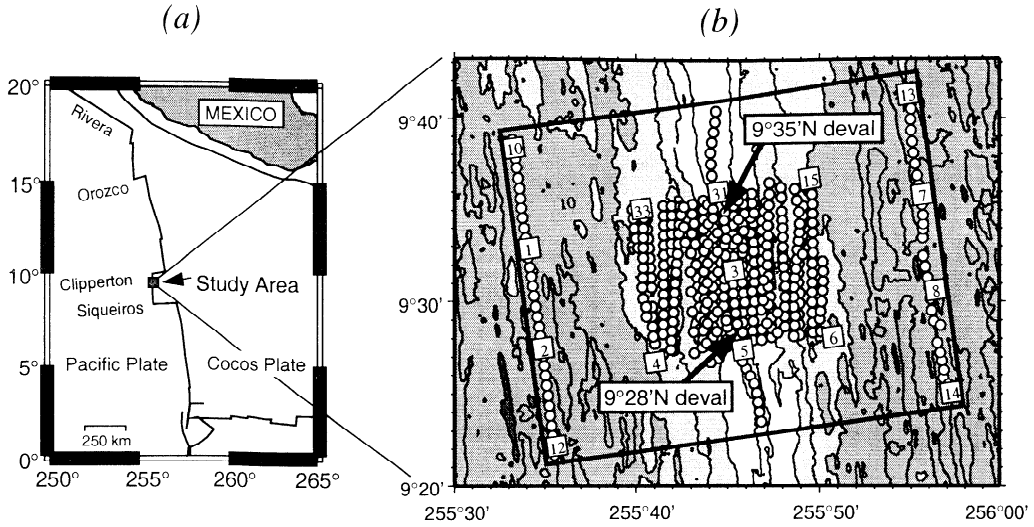

Figure 1. (a) Location of the study area (shaded box) and (b) seafloor bathymetry and geometry of the seismic experiment. Bathymetry is contoured at 100-m intervals; shading changes every 200 m. An array of 15 ocean bottom receivers, seven near-axis and eight off-axis instruments (numbered squares), recorded data from about 480 explosive sources (small circles). Box indicates the area of tomographic imaging.

lens (*dPa*), 707 diffractions below the melt lens (*dPb*), and 462 Moho- (*PmP*) and 225 mantle-turning (*Pn*) arrivals, for a total of 5296 arrivals. Previous tomography studies modeled 50% of the *Pg* arrivals [*Toomey et al.*, 1994], all *Pg* and 50% of the *dPa* and *dPb* arrivals [*Toomey et al.*, 1990], and 50% of the *Pg* and 90% of the *Pn* arrivals [*Dunn and Toomey*, 1997]. No previous modeling included *PmP* arrivals. All primary arrivals were picked using an automatic picking routine [*Takanami and Kitagawa*, 1988; *Toomey et al.*, 1994] that assigns relative uncertainties. Secondary arrivals were individually hand-picked, or in a few cases, nearby traces were stacked by cross-correlation techniques and a pick was made on the stack. Greatly aiding the identification of the arrivals is a uniform and known source signature. Picks of the secondary arrivals were assigned uncertainties of either 6, 10, 15, or 20 ms; arrivals with uncertainties >20 ms were not used. The total root-mean-square (rms) uncertainty of each phase is 7 ms for *Pg*, 11 ms for *dPa*, 13 ms for *dPb*, 13 ms for *PmP*, and 11 ms for *Pn*. The total combined data and experimental [see *Toomey et al.*, 1994] uncertainty is 12 ms.

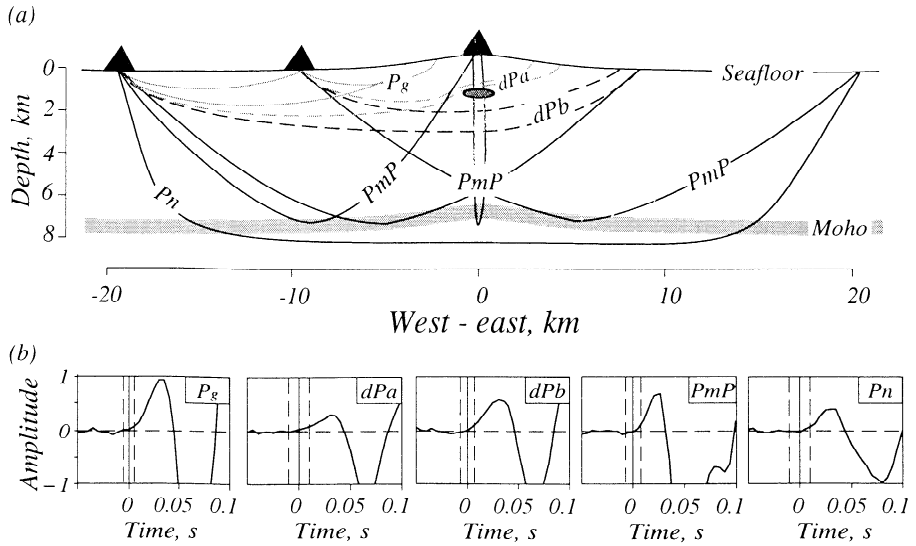

Figure 2. The observed seismic (compressional) arrivals include crustal phases (*Pg*), diffractions above the melt lens (*dPa*), diffractions below the melt lens (*dPb*), and Moho (*PmP*) and mantle (*Pn*) turning phases. (a) Illustrative ray paths for the various seismic phases recorded by receivers located on axis, 9 km off axis, and 20 km off axis. The three axial receivers recorded primary *Pg* energy that sampled the upper 4 km of crust. In addition, the northernmost and southernmost axial receivers recorded several secondary *PmP* events for shots along the rise axis. Receivers located 9 and 20 km from the rise axis each recorded *Pg*, *dPa*, *dPb*, *PmP*, and *Pn* phases. (b) From left to right, insets show example wave forms for each phase. Each instrument sampled at 250 Hz. Amplitudes are normalized to that of the first peak of the *Pg* arrival. A solid vertical line indicates the travel time pick of each arrival; vertical dashed lines indicate the pick uncertainty.

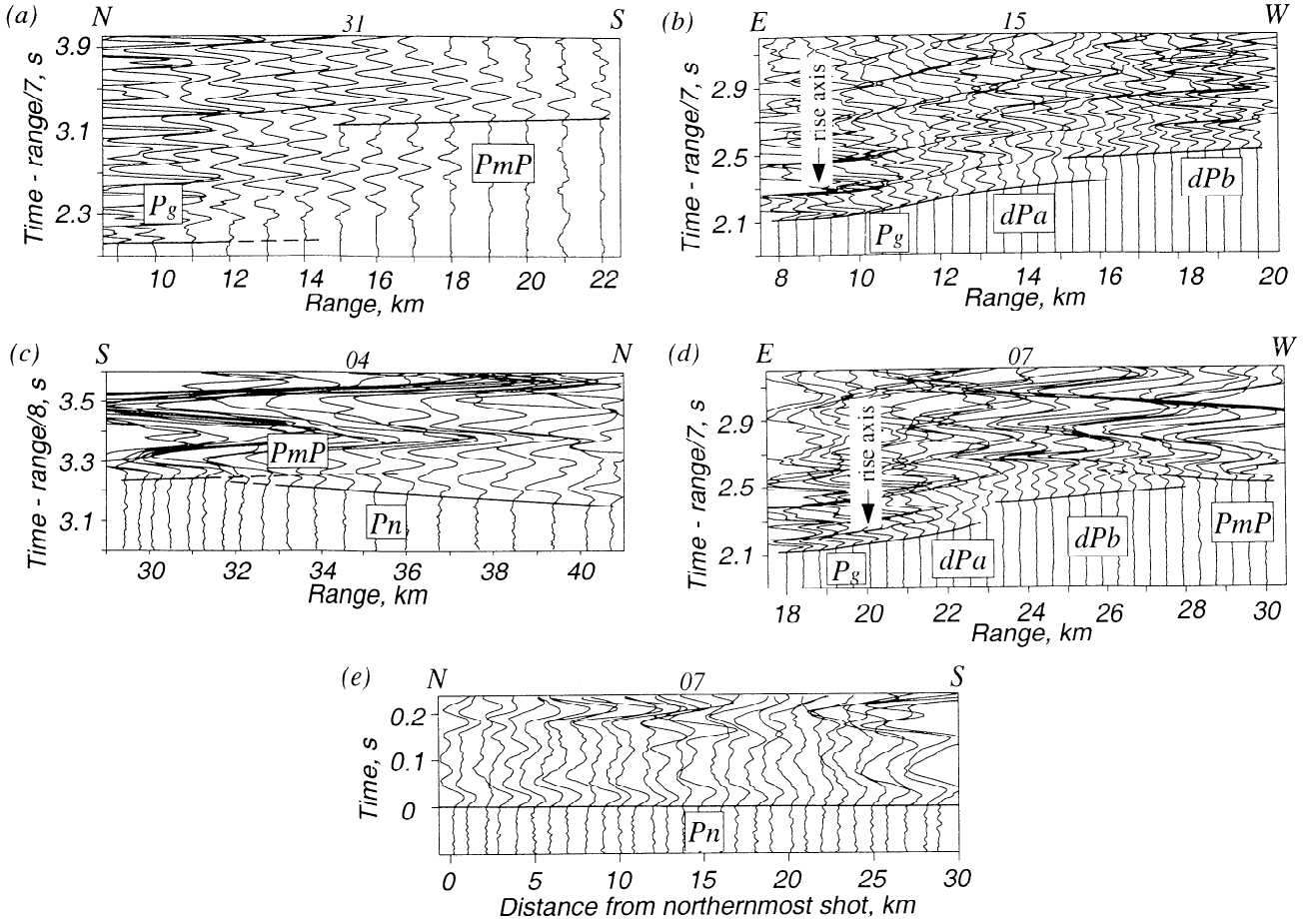

Figure 3. Example record sections. Reduced travel time versus range for (a) axial receiver 31; shots southward along the rise axis. Primary *P* wave energy (*Pg* and *dPa*) is recorded along the rise out to 12 km range. *PmP* events are observable between ranges of 15 and 22 km. (b) Receiver 15, located 9 km off axis. A line of shots obliquely (25° from the rise-perpendicular direction) crosses the rise axis. The *dPa* arrivals are detected for ray paths whose sources are up to 7 km past the rise axis (16 km total range). The *dPb* arrivals are seen in this section at ranges of ~14 to 20 km and in other sections to 28 km total range. This phase appears as a first arrival for ranges >16 km, but it is actually preceded by a *dPa* arrival whose amplitude is less than that of the background noise [*Wilcock et al.*, 1993]. (c) Receiver 4, located 9 km off axis; shots along the easternmost rise-parallel refraction line. Ray paths for these shots form a fan in map view. At ranges of 29-32 km, *PmP* arrivals are observed, and at ranges >32 km the first arrival is *Pn*. The *dPb* arrivals have too low an amplitude to be observed at these ranges. (d) Receiver 7, located 20 km off axis; a line of shots crosses the rise axis. The *dPa* arrivals are observed as first arrivals out to 3-4 km past the rise axis, at which point the amplitude does not exceed background noise. The *dPb* arrivals are observed at ranges >3 km past the rise axis and out to ~30 km total range. For ranges >25 km, a *PmP* phase appears as a secondary arrival and is easily identified by its large amplitude. (e) Receiver 7; shots along the westernmost refraction line. At these ranges (>40 km) the first arrival is *Pn*. For Figure 3e, traces are plotted by distance from the northernmost shot and are aligned at the first arrival. To maximize the visual trace-to-trace coherency, all traces are range and time adjusted to account for variations in the seafloor ray entry points.

3. Tomographic Method

We adopt an iterative stochastic inverse method to solve the tomographic problem. The method follows that of *Toomey et al.* [1994] with the modifications discussed by *Dunn and Toomey* [1997]. The procedure is as follows: given a starting model, seismic rays are computed between sources and receivers, yielding initial travel times. The problem is linearized about this prior model to obtain a set of equations mapping model perturbations into travel time residuals (differences between the measured and calculated travel times). User-adjustable constraints on the variance and smoothness of the model parameters are prescribed. A correction, obtained via a least squares procedure, is added to the prior model, and the result is used for a subsequent iteration of the forward and inverse problems. Iterations continue until the misfit between the observed and calculated travel times is minimized.

3.1. Forward Problem

The slowness model used for ray tracing is represented at grid vertices at intervals of 250 and 200 m in the horizontal and vertical directions, respectively. The grid volume has dimensions of 42 km in x (perpendicular to the rise axis), 31 km in y (along the rise axis), and 11 km in z (vertical). The origin for x and y is the center of the experiment's planform, which lies on the rise axis at 9°31.740'N and 104°14.656'W. The top of the model is conformable to the seafloor, and the model is overlain by a uniform-velocity water layer. The

model is parameterized in terms of isotropic and hexagonal-anisotropic slowness. The hexagonal symmetry system, with the symmetry axis confined to the horizontal plane, is useful for approximating the preferential alignment of anisotropic crystals in the mantle [*Dunn and Toomey*, 1997]. A shortest-path algorithm [*Moser*, 1991] is used to calculate ray paths and travel times for all seismic phases, including diffractions. To calculate the travel time between two vertices in the model, we use an approximate line integration scheme [*Moser*, 1992] that improves the accuracy of the travel times. Diffractions below the melt lens are modeled by removing grid vertices above the depth of the melt lens, forcing the shortest-path algorithm to find a minimum time path that travels beneath the lens [*Wilcock et al.*, 1993]. For the *PmP* reflections the Moho is defined on a gridded surface for which x and y grid points are the same as for the slowness grid but the z positions vary independently of the slowness grid. The reflection surface can thus have smoothly varying topography. The *PmP* paths are calculated in a two-step procedure: the paths to the Moho reflector are calculated first, and then the reflector is used to initialize ray paths that travel back to the surface [*Moser*, 1992]. For a test model with a planar Moho dipping at 25° the rms error between travel times calculated with this method and those from an analytic solution is <2 ms.

3.2. Inverse Problem

The perturbational model for isotropic slowness is defined separately on a set of vertices within the three-dimensional volume used for ray tracing. To eliminate bias in the tomographic images due to the grid representation, the perturbational grid spacing is set to less than the smallest resolvable structure as determined by Fresnel zone estimates. From the two-dimensional velocity model of *Vera et al.* [1990] we calculated a travel time field and a Fresnel zone for each phase type. The cross section of a Fresnel zone is noncircular and varies with depth. On the basis of these calculations the grid spacing of the slowness perturbation model is taken to be 0.75 km across the rise and 1.55 km along the rise and varies vertically from 0.2 km in the upper 3 km of the model to 0.5 km in the lower crust and mantle. There are a total of 35,910 model parameters. We do not invert directly for seismic anisotropy or crustal thickness variations. Instead, simple assumptions are made and tested against the data.

The solution to the problem is a trade-off between the norm of the travel time residuals, **d**, and the norm of the model, **m**, where the latter is subject to user-defined variance and smoothness constraints. We minimize the functional

$$s^2 = (\mathbf{d}-\mathbf{Gm})^{\mathrm{T}}\mathbf{C}_{\mathrm{d}}^{-1}(\mathbf{d}-\mathbf{Gm}) + \mathbf{m}^{\mathrm{T}}\mathbf{C}_{\mathrm{m}}^{-1}\mathbf{m}, \qquad (1)$$

where **G** is the Frechet matrix of partial derivatives that relates travel time misfit to model perturbations. $\mathbf{C}_{\mathrm{d}}$ is assumed to be a diagonal matrix and is made up of the individual travel time uncertainties. The upper third of $\mathbf{C}_{\mathrm{m}}$ is a diagonal matrix composed of estimates of the uncertainties in the model parameters. The lower two thirds of $\mathbf{C}_{\mathrm{m}}$ contain vertical and horizontal smoothness constraints on the model parameters. We use the method of *Toomey et al.* [1994] to apply smoothing as a Gaussian operator with decay length τ. The value of τ is chosen to be 125% of the distance between two perturbation nodes, such that only nodal positions lying within this distance are given non-zero weights in $\mathbf{C}_{\mathrm{m}}$. Vertical and horizontal model smoothnesses are controlled by independent weighting values (λ_{v} and λ_{h}, respectively), which allow user-adjustable control over the trade-off between data misfit and model smoothness. A jumping procedure [*Shaw and Orcutt*, 1985] is used to apply the model constraints to the total perturbation from the starting model. As a weighted measure of the data misfit with respect to a slowness model, we use the normalized misfit

$$\chi^2 = \left(\frac{1}{N}\right)(\mathbf{d}-\mathbf{Gm})^{\mathrm{T}}\mathbf{C}_{\mathrm{d}}^{-1}(\mathbf{d}-\mathbf{Gm}), \qquad (2)$$

where N is the number of data. If the data uncertainties are known accurately, a solution can be chosen objectively by selecting a degree of smoothness that results in a χ^2 value near one [e.g., *Constable et al.*, 1987].

4. Results

We first inverted the primary crustal data (*Pg*) for the three-dimensional, shallow crustal velocity and anisotropy structure. These data comprise 60% of the total data set, correspond to wave paths that do not interact with the axial magmatic system, and independently determine a shallow crustal model, thus providing a good starting point for subsequent inversions for deeper structure. The results were similar to those of *Toomey et al.* [1994], but the data also resolve a small amount (<4%) of anisotropy. Tomographic inversions for the deeper crustal and mantle structure used as a starting model this three-dimensional, shallow crustal model (sampled by the *Pg* arrivals at depths <4 km off axis and <1.4 km on axis) and a one-dimensional model (off-axis model of *Vera et al.* [1990]) at greater depths. As the *Pg* waves do not interact with the magmatic system, this starting model does not include the associated low-velocity region. In the Moho transition zone and mantle we assumed 7% anisotropy with the fast axis rotated 3° anticlockwise from the rise-perpendicular direction (i.e., the fast axis is oriented N101°W) on the basis of the results of *Dunn and Toomey* [1997]. The Moho reflector is taken to lie at a fixed depth of 7.5 km beneath the seafloor. We refer to this structure as the lower crustal starting model. With respect to this lower crustal starting model the data have a χ^2 misfit of 51. Details of the data misfit by seismic phase are given in Table 1 (model 1).

4.1. Average Cross-Axis Structure

The delay time data indicate anomalously low velocities throughout the middle to lower crust and mantle beneath the rise. Figure 4a presents *dPb*, *PmP*, and *Pn* travel time residuals calculated with respect to the lower crustal starting

Table 1. The χ^2 Misfit of the Data by Seismic Phase and With Respect to Different Velocity Models

Model[a]	χ^2 total	χ^2 *Pg,dPa*	χ^2 *dPb*	χ^2 *PmP*	χ^2 *Pn*
1	51	4.0	190	169	252
2	6.0	4.4	6.9	17.5	9.2
3	3.7	2.2	4.6	13.8	10.6
4	1.7	1.6	2.3	1.3	2

[a]See text for model details. Model 1, lower crustal starting model. Model 2, the two-dimensional model of Figure 5a. Model 3, the two-dimensional model of Figure 5b. Model 4, the three-dimensional model of Plate 1.

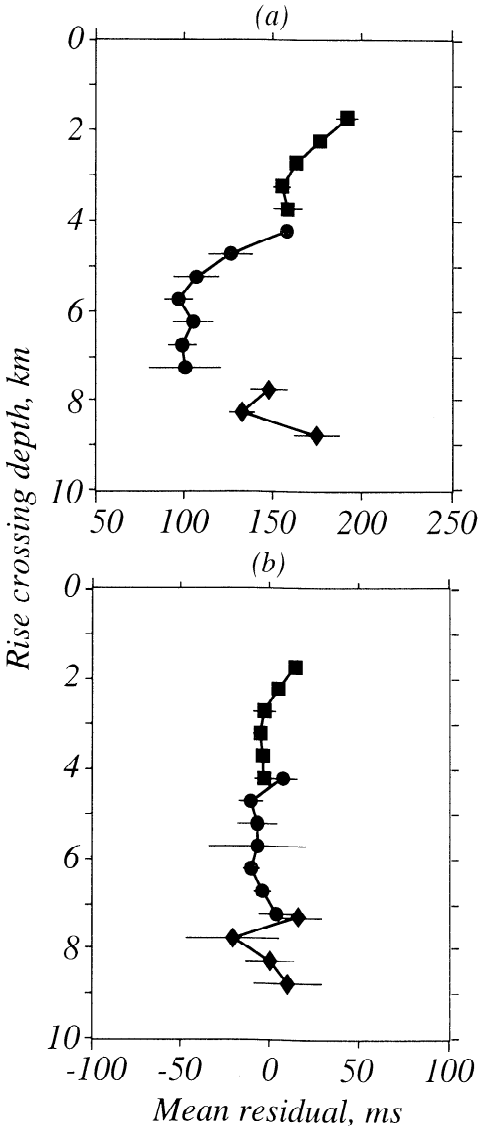

Figure 4. Average travel time residuals, with respect to (a) the lower crustal starting model and (b) the two-dimensional model of Figure 5b, for the *dPb* (squares), *PmP* (circles), and *Pn* (diamonds) data. The residuals have been sorted by their individual rise-crossing depths into 0.5-km bins, and the average of each bin is plotted along with its 95% significance level as determined by a Student's *t* test. Positive values indicate slower wave propagation than predicted by the reference model.

model and plotted by the rise-crossing depths of the ray paths. A positive residual value indicates that the velocities in the assumed model are too high. Figure 4a shows that the greatest residuals occur for rays that turn near the shallow melt lens (~2 km depth). With increasing depth of the ray turning point the magnitude of the residuals systematically decreases through the lower crust. In the shallow mantle, however, the magnitude of the residuals is similar to that observed for rays turning immediately beneath the shallow crustal melt lens. The delay time data are consistent with a low-velocity region whose magnitude (and/or width) is greatest near the shallow melt lens and the sub-Moho region and smaller in the lower crust.

Because of the nonlinear nature of the tomography problem and because the lower crustal starting model is known to differ greatly from the actual crustal structure (i.e., it does not include a low-velocity region), we adopted the conservative approach of first using the travel time data to determine two-dimensional (axially invariant) velocity models. Two-dimensional models allow us to assess the average cross-axis velocity structure of the crust and shallow mantle in the experiment area, including the width and internal structure of the low-velocity region in the lower crust. We constructed two-dimensional models in the following manner: for each iteration of the forward and inverse problems, all of the data were used to invert for three-dimensional structure, and then the total perturbation to the lower crustal starting model was averaged in the along-axis direction and recombined with the starting model. The iterations proceeded in this manner until a stable solution was obtained. This approach retained the three-dimensional structure in the shallow crust that is present in the starting model. Our preferred models, which are the result of four iterations of the forward and inverse problem, were attained for model uncertainties ($\mathbf{C}_m$) of 20% and smoothing values of $\lambda_v = \lambda_h - 75$. To achieve a good fit to both the lower crustal and mantle data, we found that λ_v across the Moho had to be reduced by half. As expected, smoother models provided similar results except velocity anomalies were of lower magnitude and the χ^2 misfit was higher. Rougher models resulted in either no significant reduction in the data misfit or a higher data misfit.

All of our tomographic inversions revealed a low-velocity volume (LVV), defined as a region in which the *P* wave velocity, V_P, is less than the starting model by >0.2 km s^{-1}. In each case, the LVV extends from 1.2 to at least 11 km depth beneath the rise axis (Figure 5). For comparison, the initial tomographic work of *Toomey et al.* [1990] resolved the LVV only to ~3 km beneath the seafloor. The maximum depth of the LVV is unconstrained in our models, but significance tests performed by *Dunn and Toomey* [1997] indicate that the *Pn* data require the LVV to extend to at least 11 km beneath the seafloor; otherwise, waves would simply propagate beneath the LVV and not be sensitive to it. At depths >9 km (or >2 km beneath the Moho), the width and magnitude of the LVV are poorly constrained and are only the minimum required to preclude a faster travel time path beneath the LVV.

We used the delay time data and our tomographic method to constrain the cross-axis width of the crustal low-velocity volume. To do so, we conducted inversions for starting models whose off-axis model uncertainties within the crust were reduced by 75% relative to those beneath the rise. By varying the location of the boundary between higher and lower uncertainties we tested whether the data are sensitive to the width of the crustal LVV. As the boundary was brought nearer to the rise axis, thereby squeezing the LVV inward, the data misfit improved up to the stage where the boundary was located 2.5 km from the rise. For squeezing half widths <2.5 km the data misfit deteriorated. Figure 5 shows the results with and without squeezing. For a squeezing half width of 2.5 km (Figure 5b) the LVV is 1-2 km narrower than without squeezing (Figure 5a). Moreover, for our preferred two-dimensional model (Figure 5b) both the final data misfit and the model norm are less than that achieved without a squeezing constraint (χ^2 of 3.7 versus 6.0, see Table 1, and the Euclidean model norm is reduced by 10%). We also tested the sensitivity of the data to the width of the mantle portion of the LVV and found that the best fitting total width is 16-18 km, as reported by *Dunn and Toomey* [1997].

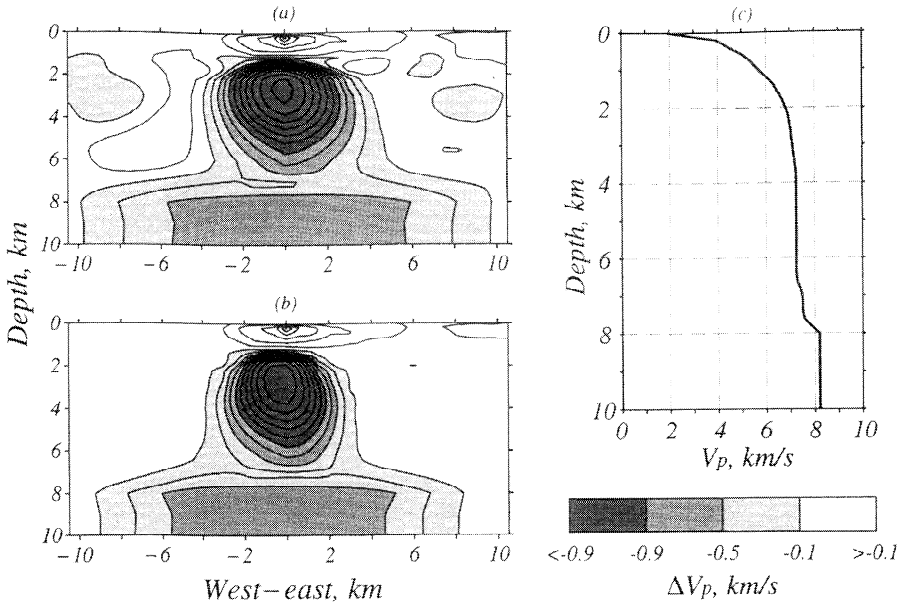

Figure 5. Results of the two-dimensional tomographic inversions. Vertical cross sections are shown for inversions (a) without and (b) with the lateral variation in prior uncertainties (see text). The contour interval is 0.2 km s^{-1}. (c) Velocity perturbations in Figures 5a and 5b are with respect to this one-dimensional model.

In our preferred two-dimensional model (Figure 5b) the cross-axis width of the top of the LVV, 5 km, is comparable to previous estimates [*Vera et al.*, 1990; *Toomey et al.*, 1990]. The velocities at the top of the LVV are ~2.0 km s^{-1} less than off-axis velocities at comparable depths and ~0.5 km s^{-1} (10%) less than determined by previous tomographic imaging [*Toomey et al.*, 1990], the result of the additional seismic phases and improved imaging techniques used here. The top of the LVV in Figure 5b also corresponds with the location of the shallow melt lens (~1.5 km depth) detected by seismic reflection [*Detrick et al.*, 1987]; the melt lens itself is not resolved by our techniques because of its small thickness relative to the seismic wavelengths (250-600 m at this depth). Figure 4b shows that the vertical trend of the data is well modeled by our preferred two-dimensional velocity structure.

The two-dimensional results provide improved constraints on the width and magnitude of the LVV in the lower crust. In previous seismic work [*Vera et al.*, 1990] the lack of any low-velocity region 10 km from the rise axis fixed the maximum full width of the crustal portion of the LVV to be <20 km. Figure 5b shows that the LVV is only 7 km wide at 5 km depth and broadens little with depth in the lower crust. The axial lower crust in our model has an average velocity of ~5.5 km s^{-1}, similar to the value estimated by *Vera et al.* [1990]. However, as evidenced from the data in Figure 4a and the inversion results, we require a positive velocity gradient in the lower crust. With increasing depth from 2 to 7 km below the seafloor, the lateral velocity contrast in the LVV in our model decreases by 1.6 km s^{-1}. In terms of absolute velocities, axial velocities increase with depth throughout the lower crust and mantle (on a scale greater than the model resolution, ~2 km; see section 4.4). As the LVV crosses from the lower crust into the mantle, the lateral velocity contrast increases by 0.5 km s^{-1} and the width of the LVV more than doubles. The vertical variations in the magnitude of the velocity anomaly within the LVV and in the width of the LVV in the crust and mantle are previously unknown features of the EPR velocity structure.

4.2. Three-Dimensional Structure

Relative to the preferred two-dimensional model (Figure 5b), the delay time data show evidence for significant along-axis variations in the structure of the axial low-velocity region. Figure 6 shows the travel time residuals as a function of rise crossing point (along-axis distance) and by seismic phase (a proxy for depth). For ray paths that cross the rise near the melt lens (*dPa* and *dPb*), in the lower crust (*PmP*), and in the mantle (*Pn*), the residuals exhibit systematic along-axis variations of 25-120 ms, with the most positive residuals generally located between two devals near 9°28'N and 9°35'N (-7 km and +6 km, respectively). For ray paths that cross the rise in the midcrust (*dPb*), there is a general trend of increasing delay to the north. While the data indicate that each of the four seismic phases (*dPa, dPb, PmP, Pn*) require along-axis variation in the LVV, since the ray paths cross the rise at a variety of depths and angles, it is difficult to determine the nature of the structure from the residual patterns alone.

To determine the three-dimensional velocity structure, we conducted several hundred inversions using a variety of inversion parameters and either the full data set or subsets of the data. Our preferred model was constructed using all of the data and a two-dimensional structure (Figure 5b) as a starting model (prior uncertainties in this model were taken to be 10%) and is the result of five iterations of the forward and inverse problem for smoothing values of $\lambda_v = \lambda_h = 75$. As expected, smoother models provided similar results except velocity anomalies were of lower magnitude and the χ^2 misfit was higher. Rougher models resulted in either no significant reduction in the data misfit or a larger data misfit. We also inverted each of the seismic phases separately and, cumulatively, obtained similar results. This test indicated that each of the seismic phases (*dPa, dPb, PmP, Pn*) requires along-axis variation in the LVV over some portion of its respective range in turning depths, a result significant at the 95% confidence level as determined by an *F* test that

compares the ratio of χ^2 misfits of the two- and three-dimensional models. Finally, we constructed models using the lower crustal starting model instead of the two-dimensional starting model. Although models were found that were consistent with the data, these models exhibited a greater degree of along-axis heterogeneity at some depths than the minimum amount required by the data. Our preferred three-dimensional model, conservatively constructed from the two-dimensional model of Figure 5b, contains the minimum amount of along-axis structure required to fit the data.

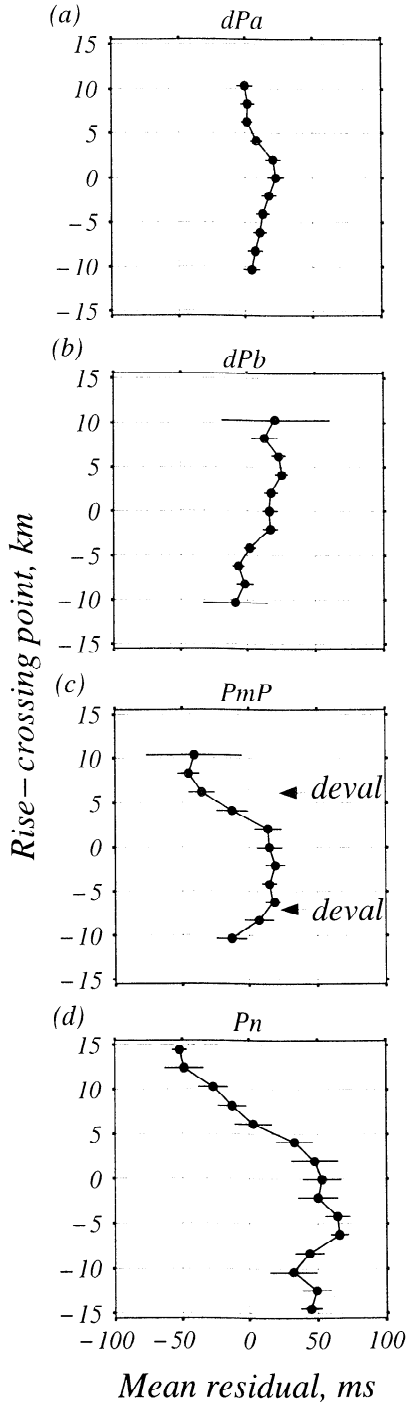

Figure 6. Average residuals for (a) *dPa*, (b) *dPb*, (c) *PmP*, and (d) *Pn* data, plotted against the rise-crossing point (y coordinate) of the wave path. Residuals are calculated with respect to our preferred axially invariant model (Figure 5b). The residuals have been sorted into 2 km bins by their individual rise-crossing points, and the average of each bin is plotted along with its 95% significance level as determined by a Student's *t* test. Positive values indicate slower wave propagation than predicted by the reference model.

Cross sections through the preferred model (Plate 1) reveal along-axis variations within the LVV, with the lowest absolute velocities located between the two devals at 9°28'N and 9°35'N. As previously reported by *Toomey et al.* [1990] and *Dunn and Toomey* [1997], significant along-axis variation exists in the uppermost part of the LVV and in the shallow mantle. In the vicinity of the shallow melt lens, at 1.2-2 km depth, the top of the LVV varies in magnitude and position with respect to the rise axis. At these depths the along-axis variation in velocity is up to 1.0 km s^{-1}. In general, the lowest velocities are centered between the two devals and are displaced 0.5-1 km to the west of the rise axis. In the mantle, at depths >7 km, velocities are up to 0.6 km s^{-1} lower between the devals than to the north or south.

New aspects of the along-axis variation in structure of the middle to lower crust beneath the EPR are revealed in our results. From ~3 to 5 (±0.5) km depth the data (a portion of both the *dPb* and *PmP* data) allow but do not require along-axis variation in the LVV. In contrast, the lowermost crust (5-7 km depth) exhibits a significant along-axis variation that is similar to that reported for the mantle and the upper part of the LVV. At these depths a variation of ≥0.4 km s^{-1} in the LVV is required by the *PmP* data, with the lowest velocities centered between the devals.

In summary, except within the depth interval 3-5 km where no variation is required, our results document that the characteristic scale of along-axis variation in velocity structure is similar from the upper mantle, through the lower crust, and upward to the top of the LVV. This scale of segmentation in the seismic structure correlates with the morphologic segmentation defined by the devals near 9°28'N and 9°35'N.

4.3. *Pn* Anisotropy and Mantle Flow Models

By analogy with studies of the Oman ophiolite [e.g., *Nicolas et al.*, 1988; *Nicolas and Boudier*, 1995; *Jousselin et al.*, 1998], the segmentation of crustal and shallow mantle isotropic velocity structure along the rise, documented by our tomographic results, may be the result of mantle diapirism. Since mantle diapirs are predicted to have a significant effect on the pattern of mantle flow and the crystallographic alignment of olivine *a* axes [*Jousselin et al.*, 1998], we evaluated the sensitivity of *Pn* delay times to two- and three-dimensional models of seismic anisotropy (Figure 7).

In previous work, *Dunn and Toomey* [1997] assumed that the fast direction of seismic anisotropy (*a* axis of olivine) was uniformly aligned in the spreading direction, consistent with two-dimensional plate-driven flow in the mantle (anisotropy due to melt bodies aligned normal to the minimum compressive stress would have a fast axis parallel to the rise axis). Figures 7c and 7d show the predicted travel time residuals for *Pn* phases versus path azimuth for models in which the fast axes of seismic anisotropy are uniformly perpendicular and subperpendicular to the rise. Structurally, a diapir is characterized by dominantly radial anisotropy in a

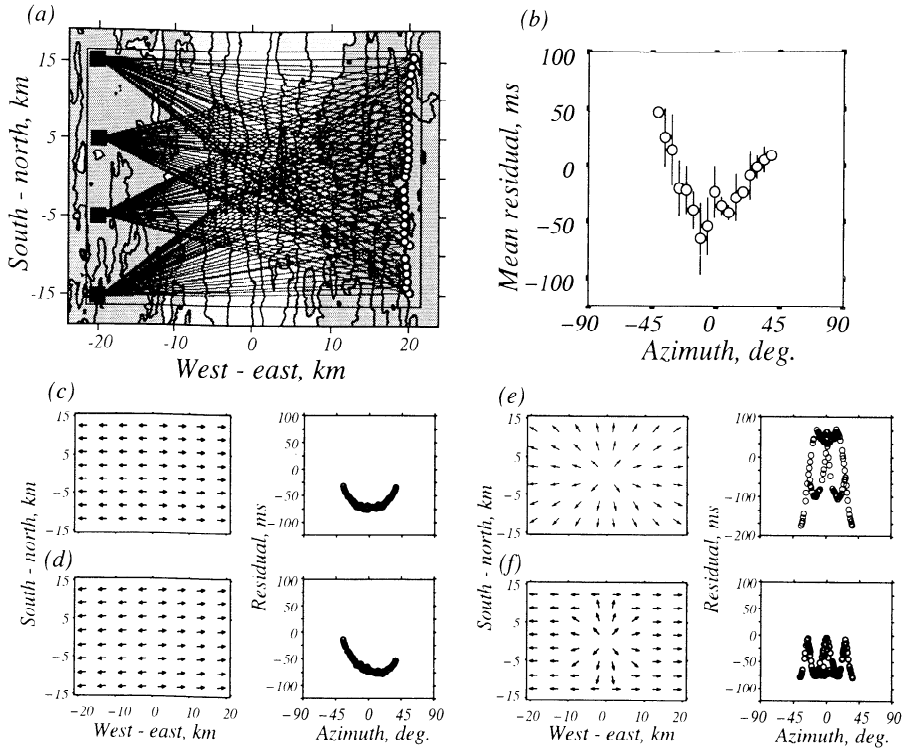

Figure 7. A comparison of the *Pn* data with synthetic data calculated for different assumptions regarding seismic anisotropy. (a) Map view of the experiment showing the shots (open circles), receivers (solid squares), and ray paths used for the comparisons. (b) Observed *Pn* travel time residuals (with respect to the two-dimensional, isotropic model shown in Figure 5b) plotted by azimuth of the ray path with respect to the rise-perpendicular direction. Positive values indicate slower wave propagation than predicted by the reference model. Delay times are shown for four receivers located 20 km to the west of the rise axis; a similar pattern occurs for receivers east of the rise. Since the data include the effects of along-axis variation in velocities beneath the rise, the data have been binned in 5° intervals and the mean of the bin is plotted along with its 95% significance level. Figures 7c-7f are map views of models of seismic anisotropy and synthetic *Pn* delay times; 7% anisotropy is assumed in each case. (c) Homogeneous anisotropy with the azimuth of the fast axis perpendicular to the rise axis. (d) Homogeneous anisotropy with the fast axis rotated 5° counterclockwise. (e) Seismic anisotropy consistent with radial flow away from the axis of a mantle diapir having a radius larger than the aperture of the experiment. (f) Seismic anisotropy consistent with radial flow away from the axis of a mantle diapir having a radius of 8 km. The form of the observed residuals in Figure 7b is most consistent with the synthetic model shown in Figure 7d.

horizontal plane of the mantle [*Jousselin et al.*, 1998]. Three-dimensional forward models of anisotropy for such upwelling patterns therefore contain a radial structure, where the region of radial anisotropy is either larger (Figure 7e) or smaller (Figure 7f) than the experiment area. In each case, the fast axis of propagation lies in a horizontal plane and the magnitude of anisotropy is assumed to be 7%. Both of the two-dimensional models of mantle flow predict U-shaped patterns, with the symmetry of the U pattern sensitive to minor (5°) variations in the azimuth of the fast axis (Figures 7c and 7d). The residuals for the diapir-like models yield a pattern that is distinct from that predicted for two-dimensional mantle flow (Figures 7e and 7f). For example, the two-dimensional models predict large delays for ray paths that cross the rise at oblique angles, as these paths travel at up to 45° to the fast axis of anisotropy. In contrast, the diapir-like models predict less delay along the same paths because the paths are aligned nearly along the fast axis of anisotropy.

The residuals of the actual data (Figure 7b) display an asymmetric U-shaped pattern consistent with two-dimensional flow and a slight rotation of the fast axis away from the predicted flow line (i.e., the NUVEL-1A spreading direction [*DeMets et al.*, 1994]). Along-axis variation in velocity structure at mantle depths, corresponding to the variability revealed in the tomographic images, gives rise to the relatively large standard deviations of the azimuthally binned data shown in Figure 7b. Although the data provide no indication that radial anisotropy exists in this area, by independently reducing the radius of the diapir and the magnitude of the along-axis component of the radial pattern we found that the data cannot distinguish between a model with uniform anisotropy and models where the diameter of the region with radial anisotropy is <2-3 km or the along-axis component of radial anisotropy is ≤2%. We conclude that a mantle diapir is not present beneath 9°30'N or, if present, does not give rise to a detectable pattern of seismic anisotropy.

4.4. Resolution

Model resolution may be evaluated by analyzing the distribution of ray paths and the reconstruction of synthetic models. The derivative weight sum (Figure 8) [*Thurber*, 1983; *Toomey and Foulger*, 1989] is a weighted sum of path lengths influencing a model parameter and provides a visual

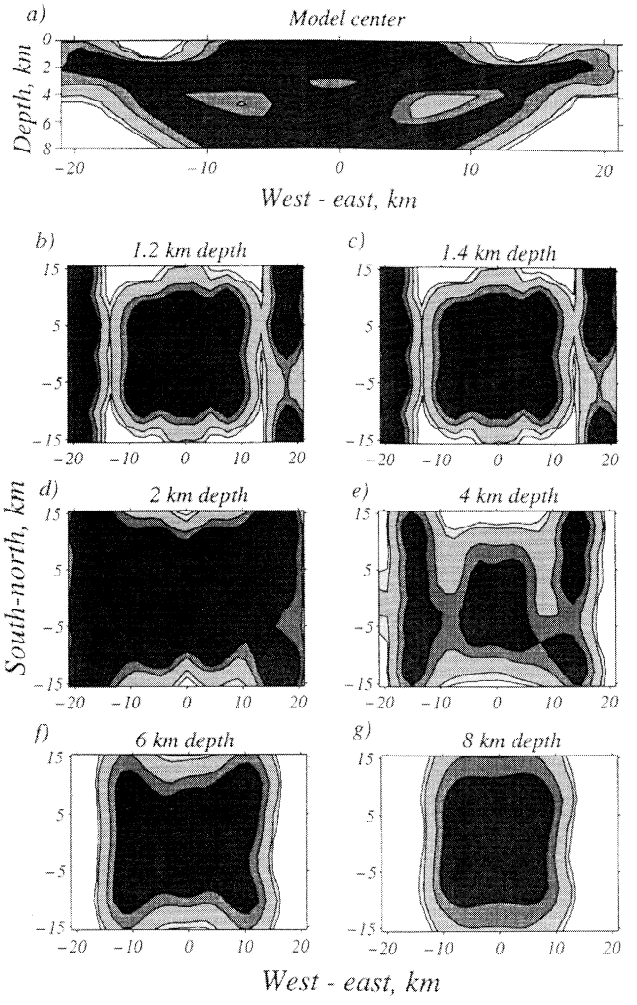

Figure 8. Vertical and map view sections of the derivative weight sum (DWS) to illustrate the ray coverage for the experiment. The DWS is contoured at values of 0.5 (low coverage, light), 1, 5, and 10 (high coverage, dark). (a) Vertical section through the model center. (b-f) Map view sections through the middle to lower crust and Moho. The ray path distribution is most complete in the 20 x 20 km^2 central region. (g) Mantle level ray density is good over a 24 x 30 km^2 area centered on the rise.

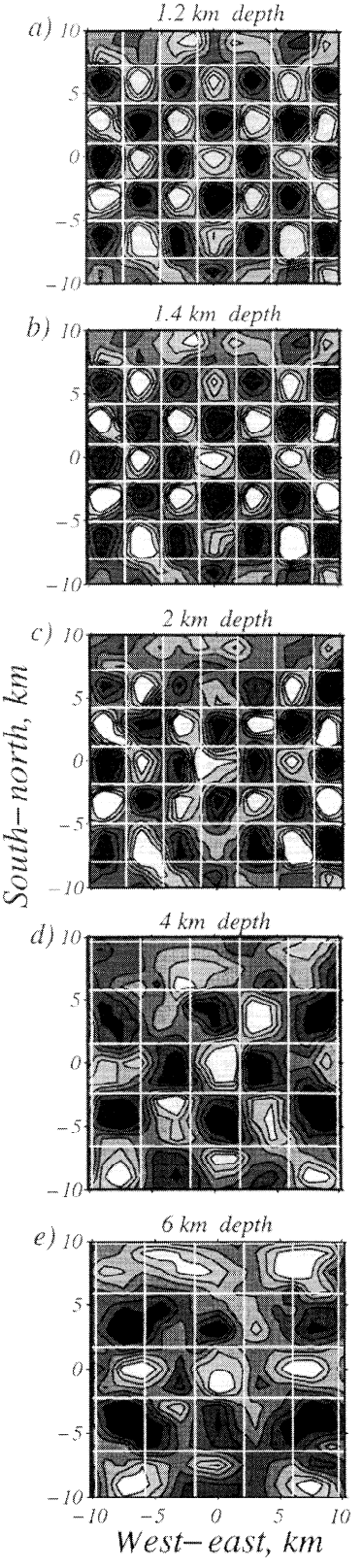

Figure 9. Results of checkerboard resolution tests. (a-e) Map view sections through the three-dimensional checkerboard model. Areas and depths of plots are as in Plate 1. White lines indicate the positions of the original anomalies. From 0 to 3 km depth the checks are cubes 3 km on each side. Below 3 km depth, the checks are 4 km in width and 3 km in height. The contour interval is 0.2 km s^{-1}.

map of the distribution of seismic rays. The ray coverage is best within a central 20 x 20 km^2 region at all depths within the crust and within a 24 x 30 km^2 region in the mantle. Ray coverage is also good beneath the outer two refraction lines in the shallow crust.

To further quantify the model resolution, we employ three-dimensional synthetic tests. Synthetic tests for the mantle (*Pn*) data were presented by *Dunn and Toomey* [1997] and are not repeated here. Our tests included synthetic checkerboard models with block sizes that varied between 2 and 5 km on a side and in all cases were 3 km in height. The checkerboard patterns do not necessarily line up with the perturbational model's grid spacing. The magnitude of the velocity difference in the blocks is ±0.5 km s^{-1} with respect to a 7 kms^{-1} background velocity. To account for the complex nature of the ray paths in the axial region (i.e., ray paths are model-dependent), we use a ray set derived from the final three-dimensional model shown in Plate 1. Because tomographic

inversions are able to detect low-velocity anomalies by ray avoidance [*Hole*, 1992], however, a fixed ray set may underrepresent the resolution in some parts of the model. From the fixed rays, travel times are computed for the synthetic models, and Gaussian noise with a standard deviation of 12 ms is added. The synthetic data are then inverted with the same model parameterization as that used with the actual data.

The results of the checkerboard tests are given in Figure 9; the areas and depths shown here match those presented in Plate 1. For depths of 1.2, 1.4, and 2 km the reconstruction of a 3-km checkerboard test (Figures 9a-9c) is remarkably good within the 20 x 20 km^2 areas shown. A smaller 2-km checkerboard pattern (not shown) was also well recovered within the innermost 12 x 12 km^2 region and beneath the outer refraction lines. Additionally, both 4- and 5-km checkerboards (not shown) were well reconstructed for a 40 x 20 km^2 region centered on the rise. For depths of 4 and 6 km, 2- and 3-km checkerboards were only partly reconstructed; better results were obtained for 4- and 5-km checkerboards. Models with 4-km blocks are shown for these depths (Figures 9d and 9e); individual blocks are well recovered in terms of their positions, but the magnitudes vary. Given that the ray set is able to reconstruct the three-dimensional blocks in the 3-5 km depth range, we conclude that the lack of along-axis variation in the tomographic image at 3-5 km depth (Plate 1e) is not due to a lack of resolution.

In general, the results must be interpreted in terms of averages of physical properties over scales of ≥2 km at all depths, inasmuch as the data do not resolve small-scale structures with sharper velocity contrasts. For example, the existence of a shallow (1.5 km depth) melt lens, as predicted by reflection surveys, cannot be resolved. We limit the discussion of the results to regions with good ray coverage.

Our modeling has been based on the assumption of a constant-thickness crust. Imaging of the lower crust, which is constrained by the *PmP* reflection data, may thus be affected by unmodeled topography on the Moho. An independent crustal thickness estimate for our experiment area, obtained from seismic refraction profiles, indicates that the crust thickens by 400-500 m from the north to the south [*Canales et al.*, 1999]. Across the rise, seismic reflection experiments performed in our area detected <500 m variation in the crustal thickness [e.g., *Detrick et al.*, 1987; *Vera et al.*, 1990; *Barth and Mutter*, 1996]. Here we test our assumption of a constant-thickness crust by altering the crustal thickness in the starting model, recomputing the seismic structure, and comparing the new model to the results of Plate 1.

We first modified the starting model to incorporate the crustal thickness estimates of *Canales et al.* [1999]. Since these measurements were made along single lines located 20 km to either side of the rise, we interpolated the structure between the lines to obtain a two-dimensional surface for the Moho. The data were reinverted with this new starting model. The resulting tomographic image is similar to that shown in Plate 1, except in the mantle at distances >10 km north of the experiment center, where velocities are ~0.2 km s^{-1} higher. Next, to determine the influence of cross-axis changes in Moho depth we assumed that the Moho is either 500 m deeper or shallower beneath the rise than away from the rise. As the majority of the *PmP* data have reflection points 3-4 km from the rise axis, the region with a deeper or shallower Moho was taken to extend to 5 km to either side of the rise axis (in that a transition closer to the rise axis would have no effect on the *PmP* travel times). The maximum difference between a model produced with an axially deeper or shallower Moho and one without is a ~0.2 km s^{-1} increase in velocity in the subaxial lower crust; the average difference in the subaxial lower crust (4-7 km depth) is ~0.05 km s^{-1}. The data misfit for the new models is somewhat higher; the probability that a model with a constant-thickness crust fits the data better than one with an axially deeper or shallower Moho is 80%. Any along-axis variation in crustal thickness within 5 km of the rise axis may affect the observed along-axis variation in velocity structure in the lower crust. To test this possibility, we assumed that along-axis variation in Moho depth has a form similar to the *PmP* delay time pattern shown in Figure 6c. This variation is scaled to produce models with a north-to-south variation in Moho topography of 200-1000 m. Tomographic inversions for models with 200-500 m of variation are similar to that shown in Plate 1. Models with 600 m or more variation did significantly reduce the along-axis variation shown in Plate 1f but also resulted in significantly poorer fits to the data. We conclude that Moho depth variations of ≤500 m are allowed by the data, but any such variations do not significantly affect our tomographic images of the subaxial velocity structure.

5. Interpretation of the Seismic Structure

The seismic tomography results allow us to estimate the physical properties of the crust and shallow mantle. We first attempt to explain the observed LVV by the effect of lateral variations in subsolidus temperature on seismic velocities. Because the LVV cannot be completely explained by a thermal anomaly, we then estimate the amount of melt required to produce the remaining velocity reduction.

5.1. Thermal Anomaly

At subsolidus temperatures, seismic velocities depend on temperature through both anharmonic and anelastic effects. Anharmonic effects do not entail seismic energy loss and are independent of frequency. Anelasticity entails energy loss, is frequency-dependent, and is the result of internal relaxation of the medium during the passage of a seismic wave [e.g., *Karato and Spetzler*, 1990]. The observation of low Q values beneath the EPR at 9°30'N [*Wilcock et al.*, 1995] is evidence for anelasticity associated with the LVV in our tomographic images. The relaxation mechanisms for seismic anelasticity are thermally activated, and a change in seismic velocity with temperature depends on the frequency dependence of attenuation. Unfortunately, this frequency dependence is poorly understood for crustal rocks at near-solidus temperatures, and the bandwidth employed in the tomography experiment is insufficient to characterize the relationship. Because of this uncertainty, we estimate the maximum and minimum effects of temperature on seismic velocities by computing thermal models where anelasticity has the greatest and least effect.

Anelasticity can significantly increase the temperature derivative of seismic velocity, with the result that the magnitude of a temperature anomaly that is estimated from a velocity anomaly is reduced. After *Karato* [1993],

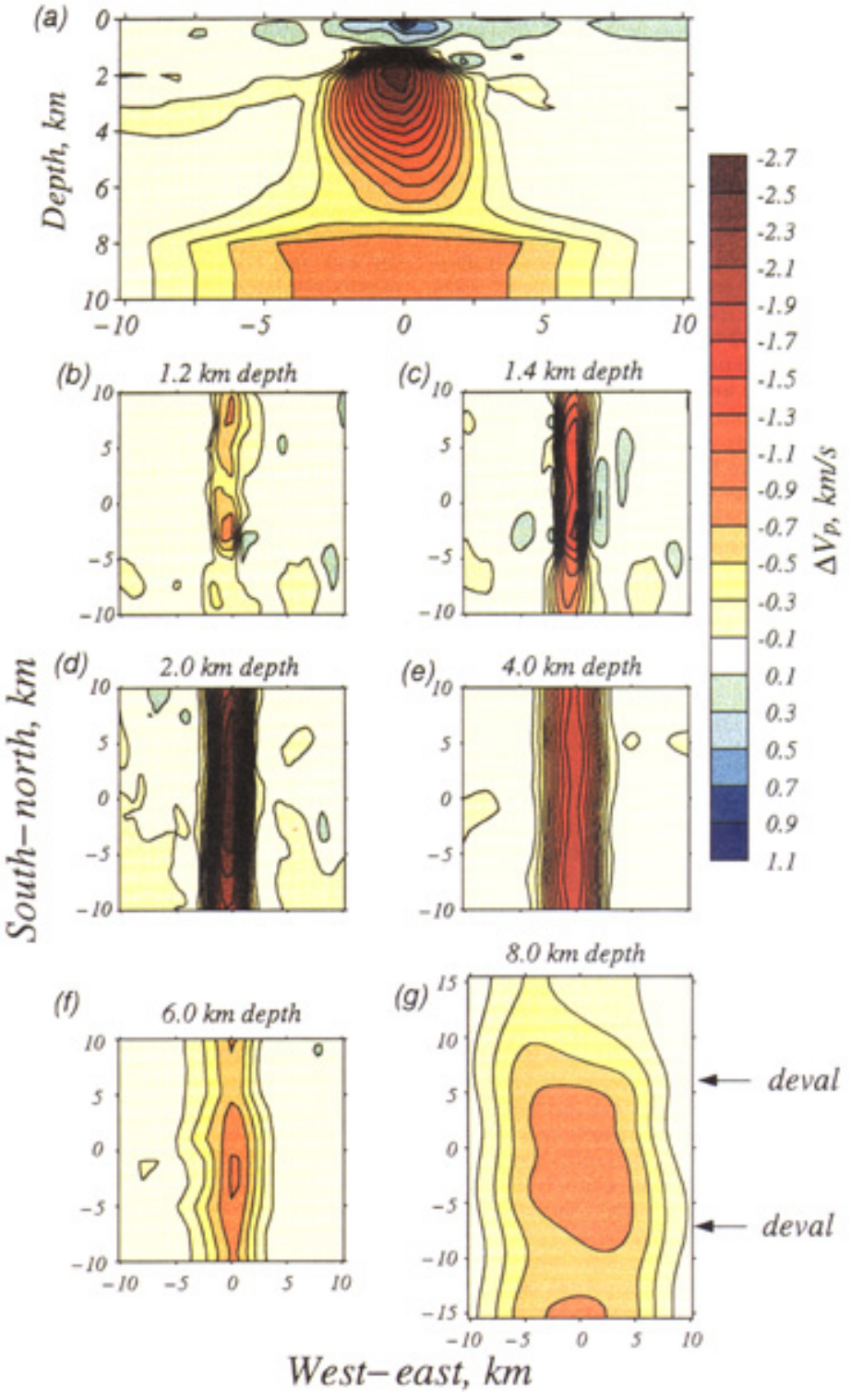

Plate 1. Final tomographic model; perturbations are shown with respect to a one-dimensional model (Figure 5c) and are contoured at intervals of 0.2 km s^{-1}. (a) Vertical section through the center (9°31.74'N) of the model. (b-g) Map-view sections taken at 1.2, 1.4, 2, 4, 6, and 8 km depth beneath the seafloor, respectively. Plot areas have been reduced, with respect to the total experiment area, such that only those areas with good ray coverage and resolution are shown.

$$\frac{\partial \ln V_P}{\partial T} = \left.\frac{\partial \ln V_P}{\partial T}\right|_{\text{anharmonic}} - F(\kappa)\left(\frac{Q^{-1}(f,T)}{\pi}\right)\left(\frac{H^*}{RT^2}\right), \quad (3)$$

where $F(\kappa) = (\pi\kappa/2)\cot(\pi\kappa/2)$, Q^{-1} is the reciprocal of the specific quality factor, f is frequency, κ is the power law exponent of the frequency dependence of Q ($Q \sim f^{\kappa}$), T is absolute temperature, R is the universal gas constant, and H^* is the activation enthalpy for seismic attenuation. Because of the spatial dependence of H^*, T, and Q, the anelastic component of the temperature derivative of seismic velocity (the second term in equation (3)) is spatially variable. Far from the rise, where Q is >500, the effect of anelasticity is negligible. Beneath the rise, where Q is 25-100, the anelastic term is significant. The largest sources of uncertainty are H^* and κ for the crust. For H^* we use a value based on the activation energy for creep, provided in Table 2, which may be similar to that for seismic attenuation [e.g., *Karato and Spetzler*, 1990]. The importance of the anelastic term increases as κ becomes small and F approaches 1. Laboratory studies suggest a weak frequency dependence in which κ = 0.1-0.3 and F = 0.92-0.99 for $f = 10^{-8}$ to 1 Hz [*Karato and Spetzler*, 1990]. Above 1 Hz, there is some suggestion that Q in the mantle has a linear dependence on f [*Solomon and Toksöz*, 1970; *Anderson and Given*, 1982]. Since these studies are not directly applicable to the conditions of our experiment, however, we estimate the maximum effect of the anelastic term by setting F = 1 and substitute the appropriate values from Table 2 into equation (3). As an example, for Q = 100 and T = 1370 K, then $\partial \ln V_P/\partial T$ = -14 x10^{-5} K^{-1} for the crust and -16 x10^{-5} K^{-1} for the mantle, values 70% and 160% larger than the anharmonic term for the derivative, respectively.

We derive two thermal models from the velocity structure shown in Plate 1. In the first model we assume anharmonic effects only, whereas in the second we include the effects of anelasticity. These models approximate the minimum and maximum contributions of temperature to the LVV. Further measurements of the effects of subsolidus temperature on frequency-dependent seismic velocities are required to narrow the range of acceptable models. To estimate a thermal structure, the velocity perturbation model is used to calculate perturbations to a reference, off-axis, one-dimensional thermal model [*Henstock et al.*, 1993]. Since subaxial temperatures are not expected to exceed ~1150°C [*Sinton and Detrick*, 1992], we attempt to explain as much of the LVV as possible by a temperature anomaly for which a 1150°C cutoff temperature is not exceeded (to explain the full magnitude of the velocity anomaly by temperature alone, temperatures in excess of 4000°C are required). Raising the cutoff temperature by 100°C or lowering the reference model by 100°C explains <0.1 km s^{-1} additional velocity anomaly. To construct the anharmonic model, only the first term of (3) is used. To construct the anelastic model, we used the Q structure of *Wilcock et al.* [1995] along with the appropriate values from Table 2 substituted into (3). For this second model the thermal structure was computed iteratively, since the anelastic temperature derivative is itself temperature-dependent. Beginning with the reference thermal model, the result of each iteration was used to compute new temperature derivatives and a new thermal structure. Iteration was ended when differences between the current and previous iterations were everywhere <10°C. The two end-member thermal models are shown in Figures 10a and 10b.

Neither of the two thermal models can explain fully the magnitude of the velocity anomaly. At least 60% of the crustal portion and 90% of the mantle portion of the low-velocity anomaly cannot be explained by temperature alone. At least 55% of the crustal width and 95% of the mantle width of the LVV cannot be explained by temperature alone. Melt must therefore be present to explain a significant portion of the LVV. Figure 10 shows that at 4 km depth the full width of the region required to contain melt is ~4-6 km. In the anelastic model the region enclosed by the 1150°C isotherm is

Table 2. Scaling Relations and Constants

Relation			Units	Comment
H^*_{crust}	=	276	kJ mol^{-1}	*Caristan* [1982]; based on creep activation energy of diabase
H^*_{mantle}	=	500	kJ mol^{-1}	*Jackson et al.* [1992]; based on the seismic anelasticity of dunite
$\left(\frac{\partial \ln V_P}{\partial T}\right)_{crust,anharmonic}$	=	-8.1 x 10^{-5}	K^{-1}	*Christensen* [1979]
$\left(\frac{\partial \ln V_P}{\partial T}\right)_{mantle,anharmonic}$	=	-6.2 x 10^{-5}	K^{-1}	*Isaak* [1992]
$\left(\frac{\partial \ln V_P}{\partial \phi}\right)_{spheres}$	=	0.8	—	*Schmeling* [1985]; for both unrelaxed and relaxed cases
$\left(\frac{\partial \ln V_P}{\partial \phi}\right)_{films,unrelaxed}$	=	2.0	—	*Schmeling* [1985]; α = 0.05
$\left(\frac{\partial \ln V_P}{\partial \phi}\right)_{films,relaxed}$	=	3.0	—	*Schmeling* [1985]; α = 0.05

ϕ is melt fraction.

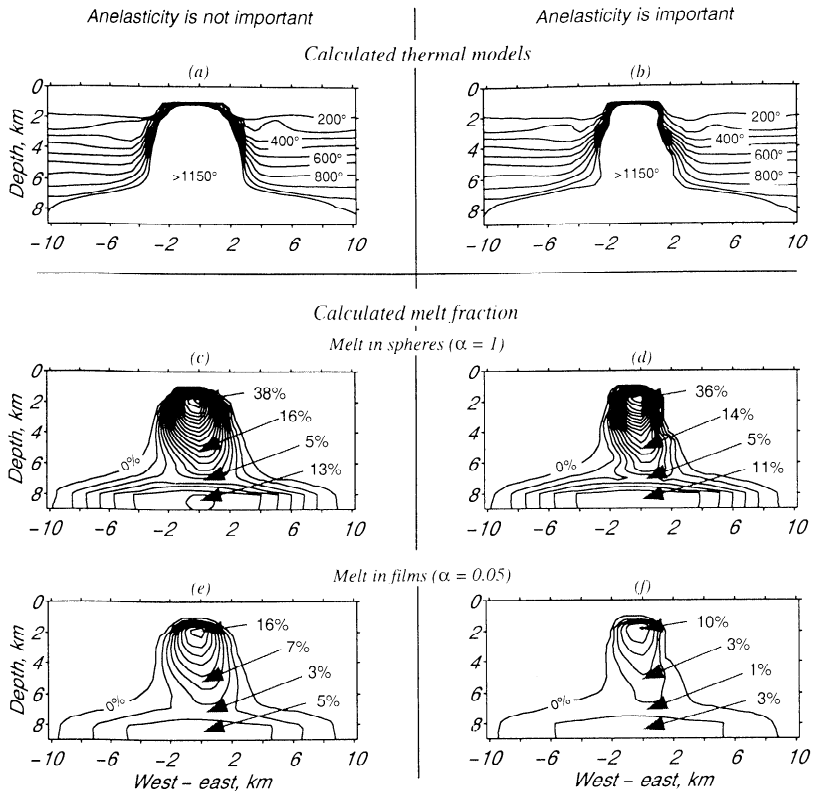

Figure 10. Temperature and melt fraction models computed from the tomographic image. Temperature is contoured at 100°C, and melt fraction is contoured at 2%. (a) Temperature model assuming anharmonic effects alone. (b) Temperature model assuming both anharmonic and anelastic effects. (c and d) Estimated melt fractions for models that include anharmonic (Figure 10c) and anharmonic plus anelastic effects (Figure 10d) and for which the melt is assumed to reside in spherical, or large aspect ratio, pockets. (e and f) Similar to Figures 10c and 10d, but for melt residing in thin pockets.

up to 2 km narrower than in the anharmonic model. Since the crustal portion of the LVV has strong lateral velocity gradients and does not extend far off-axis, in both models the off-axis crustal isotherms are relatively flat and steepen very quickly within 3 km of the rise. Our results suggest that the crustal level thermal anomaly extends <4 km from the rise. The mantle level anomaly extends to over twice this value.

5.2. Melt Anomaly

An estimate of the melt fraction within the low-velocity volume depends on the shape distribution of the melt [*Mavko*, 1980; *Schmeling*, 1985], any preferred orientation of the melt pockets [*Mainprice*, 1997], and perhaps melt-related anelasticity. Shear-stress-induced melt "squirt" between interconnected melt pockets is generally considered to cause relaxation and seismic absorption for small values ($\sim 10^{-2}$) of the pocket aspect ratio α, defined as the ratio of the semiminor to semimajor axes of a spheroidal melt pocket [e.g., *Schmeling*, 1985]. We do not specifically treat the seismic frequency dependence of melt-related attenuation but instead assume unrelaxed and relaxed conditions to provide the minimum and maximum affects of melt-related anelasticity. Laboratory studies of partially molten mantle rocks suggest aspect ratios of ~0.05 [*Faul et al.*, 1994]. Textural studies of the mantle and gabbroic sections in the Oman ophiolite suggest aspect ratios of about 0.3 [*Jousselin and Mainprice*, 1998] and 0.25 [*Lamoureux et al.*, 1999], respectively. In addition, fully or partially molten sills with aspect ratios of <0.1 may exist in the lower gabbroic section and Moho transition zone [*Kelemen et al.*, 1997; *Korenaga and Kelemen*, 1997]. We thus assume 0.05 as a lower bound and 1.0 (spherical) as an upper bound on the aspect ratio of melt pockets (aspect ratios of 0.2-1.0 will give about the same percentage melt per percent velocity reduction [*Schmeling*, 1985]). To calculate the melt fraction models, we use the method of *Schmeling* [1985] and assume that the effect of the melt pockets on seismic velocity is similar for both crustal and mantle rocks. Furthermore, because the elastic weakening effect is scale invariant, the dimensions of these pockets may range from grain boundary films to sills, as long as their dimensions are much less than the seismic wavelength. As we did not detect seismic anisotropy associated with the crustal magmatic system and the mantle anisotropy suggests alignment of anisotropic crystals by ridge spreading and not a preferred direction of melt alignment, we assume that melt pockets are randomly oriented. Our estimates of melt fraction are made from that portion of the seismic anomaly, enclosed within the 1150°C isotherm calculated above, that is not attributed to a velocity reduction due to temperature. An upper bound on melt fraction is obtained from the anharmonic temperature model and by assuming spherical melt pockets at unrelaxed conditions (Figure 10c). A minimum bound on the melt fraction is obtained from the temperature model that includes anelastic as well as anharmonic effects and by assuming that melt

resides in randomly oriented, thin pockets at relaxed conditions (Figure 10f). Intermediate models were also computed to show separately the effects of anelasticity and melt geometry (Figures 10d and 10e). Although we have assumed a constant temperature of 1150°C beneath the rise for these melt fraction calculations, temperature may increase with depth in the lower crust, say from 1150°C at the melt lens to 1250°C at the Moho. Such a vertical gradient would have a negligible effect (<1%), however, on our estimates of the lower crustal melt fraction.

Our results place new constraints on the distribution and relative amount of melt within the axial magmatic system. Comparing the models in Figures 10c-10f, the geometry of melt pockets has greater effect than anelasticity on our estimates of the amount of melt present, while the effect of subsolidus anelasticity is important in estimating the width of the region containing melt. In the absence of improved constraints on the in situ geometry of melt pockets or such additional data as S wave observations, we are unable to predict the absolute amount of melt present to better than a factor of 4. Nevertheless, we can constrain the relative distribution of melt within the magmatic system for a given assumption on melt geometry. In each of the melt fraction models, there are two regions directly beneath the rise axis with elevated melt fractions. One is at the top of the LVV and near the shallow melt lens imaged by seismic reflection studies [e.g., *Detrick et al.*, 1987], and one is in the Moho transition zone and shallowmost mantle. In all models the least amount of melt is consistently found in the lowermost crust.

It is difficult to derive a physical model from the seismic results in which the melt fraction does not decrease with depth in the lower crust, although other effects may partially explain the observed positive velocity and Q gradients in the lower crust. For example, some of the estimated melt reduction with depth (~2-4%) may be accounted for by anelastic effects alone (compare Figures 10e and 10f). In particular, if the melt fraction and aspect ratio stay the same but the relaxation state changes with depth (e.g., connected melt pockets to unconnected melt pockets), then velocities and Q would increase slightly and estimated melt percentages for the lower crust could be higher by ~3% than shown in Figure 10f. On the other hand, vertical variations in the aspect ratio may partly explain the increase in velocity with depth. For example, comparing Figures 10c and 10f, if the dominant aspect ratio of randomly oriented melt bodies increases with depth, then the increases in both V_P and Q could be partly explained without a corresponding decrease in melt fraction [see also *Schmeling*, 1985, Figure 11]. If, as suggested by ophiolite studies, the distribution of melt pockets is anisotropic (vertically aligned beneath the melt lens and horizontally aligned in the lower crust [*Mainprice*, 1997; *Lamoureux et al.*, 1999]), such a pattern could also partly explain the increase in velocity with depth. None of these scenarios, however, can completely explain the relatively high velocities in the lower crust.

In the rise-parallel direction our results suggest that more melt is present between the 9°28'N and 9°35'N devals than to the north or south. In Figure 11 we present horizontal slices at 2, 4, 6, and 8 km depth through the melt fraction models of Figures 10c and 10f (models with the maximum and minimum amount of melt, respectively). As our experiment was located far from tectonic offsets of the rise that could influence the thermal structure, the observed rise-parallel variation in seismic structure is consistent with variations in the melt fraction. An exception is at the top of the LVV (above the shallow melt lens), where spatial variations in hydrothermal circulation may produce large along-axis variations in temperature. The estimated melt fraction varies by as much as a factor of 3 along the rise, with more melt observed between the devals at 2, 6, and 8 km depth but not at 4 km depth.

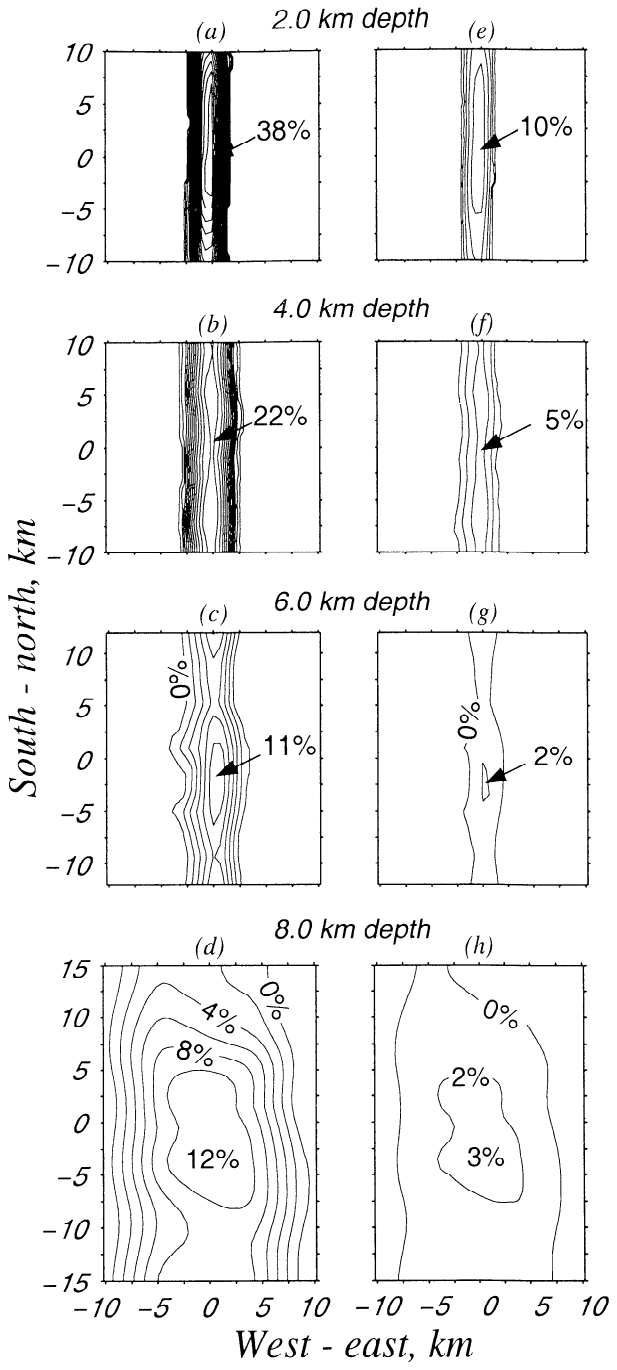

Figure 11. Maps of the along-axis variation in the estimated melt fraction. Horizontal sections are taken at depths of 2, 4, 6, and 8 km. (a-d) For model shown in Figure 10c (i.e., maximum predicted melt). (e-h) For the model shown in Figure 10f (i.e., minimum predicted melt).

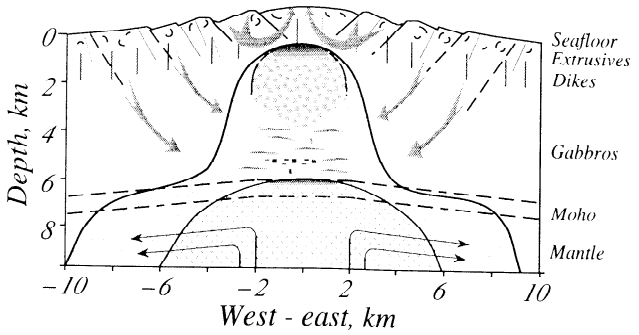

Figure 12. Schematic view of the magmatic system beneath the EPR near 9°30'N. See text for discussion. Arrows indicate hydrothermal circulation. Stippled regions indicate the presence of melt.

6. Discussion

Our results place improved constraints on the width of the melt-containing region in the crust of a fast spreading ridge. Some investigators have previously suggested that the width of the melt-containing region decreases with depth in the lower crust [e.g., *Vera et al.*, 1990], whereas others have suggested that it substantially increases in the lower crust, from ~2 km to 15-20 km full width [e.g., *Harding et al.*, 1989; *Caress et al.*, 1992; *Crawford et al.*, 1999]. Studies of the Oman ophiolite, believed to have formed in a fast spreading environment [e.g., *Nicolas*, 1989], have also led to suggestions of narrower [e.g., *Gregory and Taylor*, 1981; *Pallister and Hopson*, 1981] and wider [e.g., *Nicolas*, 1989] lower crustal widths than upper crustal widths. In cross section the region estimated to contain melt in our model (Figures 10 and 12) extends from ~1.4 km to at least 11 km below the seafloor. The full width of this region is ~5 km near the top, similar to previous estimates [*Vera et al.*, 1990; *Toomey et al.*, 1990], increases to no more than 7 km in the lower crust, and then more than doubles in width as it crosses into the mantle. Our results show that the lower crustal width of the melt-containing region is only slightly wider than the width at its top. To our knowledge, no previous model has included a substantial increase in width of the high-temperature and melt-containing regions from the lower crust to the mantle.

The width of the thermal anomaly and the region containing melt are relative indicators of the efficiency with which heat is removed from the axial region. The thermal models (Figure 10) show that anomalously high temperatures are restricted to a relatively narrow region, such that at distances >4 km from the rise axis, isotherms are approximately horizontal. Since the inferred isotherms do not conform to the predictions of a conductively cooled layer, heat removal near the rise must be relatively efficient throughout the crust (see Figure 12). Lower crustal hydrothermal circulation has been suggested from studies of the Oman ophiolite, which indicate that heat removal by high-temperature fluid circulation occurs to depths of 5-6 km [*Gregory and Taylor*, 1981; *Nehlig and Juteau*, 1982], although the proximity of this circulation to the ridge was not constrained by these studies. Our estimated thermal anomaly substantially increases in width as it crosses into the mantle, suggesting that heat removal at Moho and mantle depths is less efficient than that in the crust. Near the Moho, the deposition of alteration products from reaction of seawater with mantle minerals may clog the hydrothermal system [*Wilcock and Delaney*, 1996], lowering the efficiency of heat removal at these depths.

The tomographic results indicate that significant amounts of melt accumulate at two levels in the magmatic system. One is at the top of the system, within the shallow to middle crust, while the other is within the Moho transition zone and uppermost mantle. We refer to these regions as the upper and lower melt reservoirs, respectively. The upper reservoir is capped by a fully or mostly molten melt lens at ~1.5 km depth [*Detrick et al.*, 1987; *Kent et al.*, 1993]. The highest melt fractions in our model are within the upper reservoir, whereas the lower reservoir contains a lower melt fraction distributed over a broader cross-sectional area. By volume, however, there may be up to ~40% more melt in the lower reservoir than in the upper reservoir because of the greater width of the lower reservoir (Figure 13). These calculations do not take into account the contribution of either a crustal or a Moho level melt lens, which may add an additional ~0.1 km^3 of melt (per kilometer of rise) to each reservoir but are unresolved in our data and analysis. Our seismic results indicate that the lower crust contains the least melt, both by melt fraction and by total volume, which may indicate that it is closer to its solidus than the other regions [*Sinton and Detrick*, 1992]. Previous seismic measurements have also been used to infer relatively low melt fractions in the lower crust [*Vera et al.*, 1990; *Wilcock et al.*, 1995].

The shallow melt lens forms as buoyantly rising melt accumulates beneath a permeability or viscosity barrier at the top of the magmatic system [e.g., *Hooft and Detrick*, 1993]. In the mantle, melt migration should be rapid for melt fractions >1% [e.g., *Kohlstedt*, 1992], so our observation of a

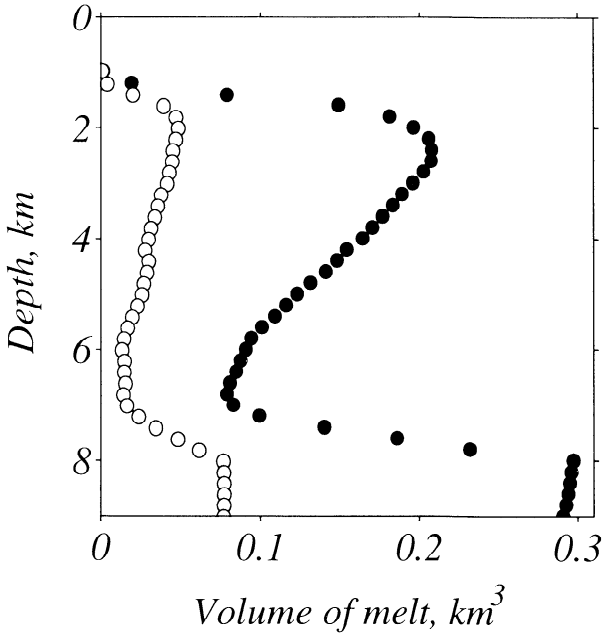

Figure 13. Volume of melt per kilometer of ridge plotted as a function of depth. Solid circles indicate model shown in Figure 10c. Open circles indicate model shown in Figure 10f. The values are calculated for 200-m depth intervals.

substantial melt fraction at this depth also indicates an impediment to upward flow. The density contrast at the Moho [*Crawford et al.*, 1999], formation of a permeability barrier due to crystallization in pore space at the base of the crust [*Kelemen et al.*, 1997; *Korenaga and Kelemen*, 1997], and changes in the stress conditions with depth and time [*Ildefonse et al.*, 1993] have been suggested as possible barriers to melt migration.

Accumulations of Moho level melt may act as a source region for the layered gabbros inferred from ophiolite studies to make up the lower crust. Chemical analyses of the lower crustal gabbros of the Oman ophiolite indicate that they are of similar composition to Moho and sub-Moho level gabbros [*Kelemen et al.*, 1997; *Korenaga and Kelemen*, 1997] and that they are "cumulates" formed by partial crystallization of a melt (<40%), after which the remaining melt was removed. In contrast, upper gabbros, dikes, and lavas have compositions of liquids in equilibrium with the lower crustal gabbros, consistent with complete crystallization of the remaining melt. Our estimation of 4-10% melt in the lower crust supports a crustal accretion model in which some fraction of the lower crust forms in situ. Furthermore, the similarity in the along-axis variation in velocity structure in the lower crust and shallow mantle suggests a common link between these two levels of the magmatic system. Our results suggest that a focused source of melt from beneath the Moho feeds melt into the lower crust, where some melt is retained (hence the along-axis variation in seismic structure at these depths). This inference is in contrast to models in which the melt is postulated to move quickly up to the melt lens [e.g., *Henstock et al.*, 1993; *Phipps Morgan and Chen*, 1993; *Quick and Denlinger*, 1993].

The evidence for higher melt fractions between the two devals at 9°28'N and 9°35'N in the upper crust [*Toomey et al.*, 1990, 1994], lower crust (this paper), and mantle [*Dunn and Toomey*, 1997] suggests that the mantle midway between the devals is presently delivering greater amounts of melt to this part of the rise than regions immediately to the north or south. This result implies either a physical focusing of melt from a homogeneous source region or a locally enhanced melt production in the mantle. In general, the mantle melt supply may be locally enhanced by mantle temperature variations [*Thompson*, 1987], source heterogeneity [*Langmuir et al.*, 1986; *Pickering and Johnston*, 1998], diapirism [*Whitehead et al.*, 1984; *Nicolas et al.*, 1994], or three-dimensional melt segregation and transport mechanisms, such as the coalescence of small-scale melt segregations, veins, dikes, or dissolution channels [e.g., *Sleep*, 1988; *Nicolas*, 1989; *Stevenson*, 1989; *Kelemen et al.*, 1995]. Because no evidence for diapiric mantle flow was found from seismic anisotropy in our data set, we suggest that mantle flow and melt migration are decoupled in the shallowmost mantle along this section of the rise. Specifically, our results indicate that mantle melt migration is focused in three dimensions, while solid flow in the mantle is essentially two-dimensional.

The absence of significant along-axis variation in melt fraction at 3-5 km depth may be indicative of a region of compaction of the crystal mush beneath the melt lens. In the crustal accretion model of *Boudier et al.* [1996] the lower crust forms by repeated injection of melt sills, whereas the middle crust forms by the downward and outward flow of crystals that form at the base of the shallow melt lens. In their model a region of compaction at 3-5 km depth may overprint along-axis variations in melt content. Alternatively, along-axis flow over this depth interval may even out any along-axis variation in melt content. It seems less likely, however, that along-axis flow would occur only at these depths, where the melt fraction is relatively low, rather than at shallower depths (~2 km), where melt fractions are higher and along-axis flow may be more feasible.

The correlation of the along-axis variation in velocity structure and estimated melt fraction found from our study with the axial morphology of the rise (devals), the variation in petrologic units [*Langmuir et al.*, 1986], the location of current and recent hydrothermal venting [*Haymon et al.*, 1991], and magnetic and gravity anomalies [*Lee*, 1995; *Lee et al.*, 1996] all support the view that focused ascent of magma has a strong local influence on the accretion of oceanic crust. Our results suggest that this focusing begins at least as deep as the upper few kilometers of the mantle. These observations are incompatible with a large, segment-scale redistribution of melt in the crust as suggested by some models [*Macdonald*, 1989; *Batiza and Niu*, 1992; *Barth and Mutter*, 1996; *Nicolas et al.*, 1996; *Wang et al.*, 1996]. Instead, our results indicate that crustal magma chambers along this portion of the EPR are replenished from the mantle at closely spaced intervals along the rise.

Acknowledgments. The computational aspects of this work benefited greatly from the assistance and resources of Chris Harrop and the Computational Science Institute at the University of Oregon. Donna Blackman, Peter Kelemen, and Yosio Nakamura provided insightful and thorough reviews. Benoît Ildefonse provided constructive comments on the submitted manuscript. The original data collection was supported by the National Science Foundation under grants OCE-8615797 and OCE-8615892. The analysis was supported by the National Science Foundation under grants EAR-9526606, ACI-9522531, EIA-9601802, and OCE-9633264 and by a University of Oregon Doctoral Fellowship.

References

Anderson, D. L., and J. W. Given, Absorption band Q model for the Earth, *J. Geophys. Res.*, *87*, 3893-3904, 1982.

Barth, G. A., and J. C. Mutter, Variability in oceanic crustal thickness and structure: Multichannel seismic reflection results from the northern East Pacific Rise, *J. Geophys. Res.*, *101*, 17,951-17,975, 1996.

Batiza, R. and Y. Niu, Petrology and magma chamber processes at the East Pacific Rise ~9°30'N, *J. Geophys. Res.*, *97*, 6779-6797, 1992.

Boudier, F., A. Nicolas, and B. Ildefonse, Magma chambers in the Oman ophiolite: Fed from the top or the bottom?, *Earth Planet. Sci. Lett.*, *144*, 239-250, 1996.

Canales, J. P., R. S. Detrick, D. R. Toomey, and W. S. D. Wilcock, Variations in crustal thickness and P-wave velocity along the East Pacific Rise between the Clipperton and Siquieros transforms from wide-angle seismic data (abstract), *Eos Trans. AGU*, *80*(46), Fall Meet. Suppl., F995, 1999.

Caress, D. W., M. S. Burnett, and J. A. Orcutt, Tomographic image of the axial low-velocity zone at 12°50'N on the East Pacific Rise, *J. Geophys. Res.*, *97*, 9243-9263, 1992.

Caristan, Y., The transition from high temperature creep to fracture in Maryland diabase, *J. Geophys. Res.*, *87*, 6781-6790, 1982.

Christensen, N. I., Compressional wave velocities in rocks at high temperatures and pressures, critical thermal gradients, and crustal low-velocity zones, *J. Geophys. Res.*, *84*, 6849-6857, 1979.

Constable, S. C., R. L. Parker, and C. G. Constable, Occam's inversion: A practical algorithm for generating smooth models from electromagnetic sounding data, *Geophysics*, *52*, 289-300, 1987.

Crawford, W. C., S. C. Webb, and J. A. Hildebrand, Constraints on melt in the lower crust and Moho at the East Pacific Rise, 9°48'N, using seafloor compliance measurements, *J. Geophys. Res.*, *104*, 2923-2939, 1999.

DeMets, C., R. G. Gordon, D. F. Argus, and S. Stein, Effect of recent revisions to the geomagnetic reversal time scale on estimates of current plate motions, *Geophys. Res. Lett.*, *21*, 2191-2194, 1994.

Detrick, R. S., P. Buhl, E. Vera, J. Mutter, J. Orcutt, J. Madsen, and T. Brocher, Multi-channel seismic imaging of a crustal magma chamber along the East Pacific Rise, *Nature*, *326*, 35-41, 1987.

Dunn, R. A., and D. R. Toomey, Seismological evidence for three-dimensional melt migration beneath the East Pacific Rise, *Nature*, *388*, 259-262, 1997.

Faul, U. H., D. R. Toomey, and H. S. Waff, Intergranular basaltic melt is distributed in thin, elongated inclusions, *Geophys. Res. Lett.*, *21*, 29-32, 1994.

Francheteau, J., and R. D. Ballard, The East Pacific Rise near 21°N, 13°N and 20°S: Inferences for along-strike variability of axial processes of the mid-ocean ridge, *Earth Planet. Sci. Lett.*, *64*, 93-116, 1983.

Garmany, J., Accumulations of melt at the base of young oceanic crust, *Nature*, *340*, 628-632, 1989.

Gregory, R. T., and H. P. Taylor, Jr., An oxygen isotope profile in a section of Cretaceous oceanic crust, Samail Ophiolite, Oman: Evidence for $\delta^{18}O$ buffering of the oceans by deep (>5 km) seawater-hydrothermal circulation at mid-ocean ridges, *J. Geophys. Res.*, *86*, 2737-2755, 1981.

Harding, A. J., J. A. Orcutt, M. E. Kappus, E. E. Vera, J. C. Mutter, P. Buhl, R. S. Detrick, and T. M. Brocher, Structure of young oceanic crust at 13°N on the East Pacific Rise from expanding spread profiles, *J. Geophys. Res.*, *94*, 12,163-12,196, 1989.

Haymon, R. M., D. J. Fornari, M. H. Edwards, S. Carbotte, D. Wright, and K. C. Macdonald, Hydrothermal vent distribution along the East Pacific Rise crest (9°09'-54'N) and its relationship to magmatic and tectonic processes on fast-spreading mid-ocean ridges, *Earth Planet. Sci. Lett.*, *104*, 513-534, 1991.

Henstock, T. J., A. W. Woods, and R. S. White, The accretion of oceanic crust by episodic sill intrusion, *J. Geophys. Res.*, *98*, 4143-4161, 1993.

Hole, J. A., Nonlinear high-resolution three-dimensional seismic travel time tomography, *J. Geophys. Res.*, *97*, 6553-6562, 1992.

Hooft, E. E. E., and R. S. Detrick, The role of density in the accumulation of basaltic melts at mid-ocean ridges, *Geophys. Res. Lett.*, *20*, 423-426, 1993.

Ildefonse, B., A. Nicolas, and F. Boudier, Evidence from the Oman ophiolite for sudden stress changes during melt injection at oceanic spreading centers, *Nature*, *366*, 673-675, 1993.

Isaak, D. G., High-temperature elasticity of iron-bearing olivines, *J. Geophys. Res.*, *97*, 1871-1885, 1992.

Jackson, I., M. S. Paterson, and J. D. FitzGerald, Seismic wave dispersion and attenuation in Aheim dunite: An experimental study, *Geophys. J. Int.*, *108*, 517-534, 1992.

Jousselin, D., and D. Mainprice, Melt topology and seismic anisotropy in mantle peridotites of the Oman ophiolite, *Earth Planet. Sci. Lett.*, *164*, 553-568, 1998.

Jousselin, D., A. Nicolas, and F. Boudier, Detailed mapping of a mantle diapir below a paleo-spreading center in the Oman ophiolite, *J. Geophys. Res.*, *103*, 18,153-18,170, 1998.

Karato, S., Importance of anelasticity in the interpretation of seismic tomography, *Geophys. Res. Lett.*, *20*, 1623-1626, 1993.

Karato, S., and H. A. Spetzler, Defect microdynamics in minerals and solid-state mechanisms of seismic wave attenuation and velocity dispersion in the mantle, *Rev. Geophys.*, *28*, 399-421, 1990.

Kelemen, P. B., N. Shimizu, and V. J. M. Salters, Extraction of mid-ocean-ridge basalt from the upwelling mantle by focused flow of melt in dunite channels, *Nature*, *375*, 747-753, 1995.

Kelemen, P. B., K. Koga, and N. Shimizu, Geochemistry of gabbro sills in the crust-mantle transition zone of the Oman ophiolite: Implications for the origin of the oceanic lower crust, *Earth Planet. Sci. Lett.*, *146*, 475-488, 1997.

Kent, G. M., A. J. Harding, and J. A. Orcutt, Distribution of magma beneath the East Pacific Rise between the Clipperton transform and the 9°17'N deval from forward modeling of common depth point data, *J. Geophys. Res.*, *98*, 13,945-13,969, 1993.

Kohlstedt, D. L., Structure, rheology and permeability of partially molten rocks at low melt fractions, in *Mantle Flow and Melt Generation at Mid-ocean Ridges*, *Geophys. Monogr. Ser.*, vol. 71, edited by J. Phipps Morgan, D. K. Blackman, and J. M. Sinton, pp. 103-121, AGU, Washington, D. C., 1992.

Korenaga, J., and P. B. Kelemen, Origin of gabbro sills on the Moho transition zone of the Oman ophiolite: Implications for magma transport in the oceanic lower crust, *J. Geophys. Res.*, *102*, 27,729-27,749, 1997.

Lamoureux, G., B. Ildefonse, and D. Mainprice, Modelling the seismic properties of fast-spreading ridge crustal low velocity zones: Insights from Oman gabbro textures, *Tectonophysics*, *312*, 283-301, 1999.

Langmuir, C. H., J. F. Bender, and R. Batiza, Petrological and tectonic segmentation of the East Pacific Rise, 5°30'-14°30'N, *Nature*, *322*, 422-429, 1986.

Lee, S. M., Tectonics of the East Pacific Rise: Studies of faulting characteristics and magnetic and gravity anomalies, Ph.D. thesis, 511 pp., Mass. Inst. of Technol./Woods Hole Oceanogr. Inst., Woods Hole, Mass., 1995.

Lee, S. M., S. C. Solomon, and M. A. Tivey, Fine-scale crustal magnetization variations and segmentation of the East Pacific Rise, 9°10'-9°50'N, *J. Geophys. Res.*, *101*, 22,033-22,050, 1996.

Macdonald, K. C., Tectonic and magmatic processes on the East Pacific Rise, in *The Geology of North America*, vol. N, *The Eastern Pacific Ocean and Hawaii*, edited by E. L. Winterer, D. M. Hussong, and R. W. Decker, pp. 93-110, Geol. Soc. of Am., Boulder, Colo., 1989.

Mainprice, D., Modelling the anisotropic seismic properties of partially molten rocks found at mid-ocean ridges, *Tectonophysics*, 279, 161-179, 1997.

Mavko, G. M., Velocity and attenuation in partially molten rocks, *J. Geophys. Res.*, *85*, 5173-5189, 1980.

Moser, T. J., Shortest path calculation of seismic rays, *Geophysics*, *56*, 59-67, 1991.

Moser, T. J., The shortest path method for seismic ray tracing in complicated media, Ph.D. thesis, Inst. of Geophys., Utrecht Univ., Utrecht Netherlands, 1992.

Mutter, J. C., G. A. Barth, P. Buhl, R. S. Detrick, J. Orcutt, and A. Harding, Magma distribution across ridge-axis discontinuities on the East Pacific Rise from multi-channel seismic images, *Nature*, *336*, 156-158, 1988.

Nehlig, P., and T. Juteau, Flow porosities, permeabilities, and preliminary data on fluid inclusions and fossil thermal gradients in the crustal sequence of the Samail ophiolite (Oman), *Tectonophysics*, *81*, 319-339, 1982.

Nicolas, A., *Structures of Ophiolites and Dynamics of Oceanic Lithosphere*, 367 pp., Kluwer Acad., Norwell, Mass., 1989.

Nicolas, A., and F. Boudier, Mapping oceanic ridge segments in Oman ophiolites, *J. Geophys. Res.*, *100*, 6179-6197, 1995.

Nicolas, A., and M. Rabinowicz, Mantle flow pattern at oceanic spreading centres: Relation with ophiolitic and oceanic structures, in *Opiolites and Oceanic Lithosphere*, *Geol. Soc. Spec. Publ.*, *13*, 147–151, 1984.

Nicolas, A., G. Ceuleneer, F. Boudier, and M. Misseri, Structural mapping in the Oman ophiolites: Mantle diapirism along an oceanic ridge, *Tectonophysics*, *151*, 27-56, 1988.

Nicolas, A., F. Boudier, and B. Ildefonse, Evidence from the Oman ophiolite for active mantle upwelling beneath a fast-spreading ridge, *Nature*, *370*, 51-53, 1994.

Nicolas, A., F. Boudier, and B. Ildefonse, Variable crustal thickness in the Oman ophiolite: Implications for oceanic crust, *J. Geophys. Res.*, *101*, 17941-17950, 1996.

Pallister, J. S., and C. A. Hopson, Samail ophiolite plutonic suite: Field relations, phase variation, cryptic variation and layering, and a model of a spreading ridge magma chamber, *J. Geophys. Res.*, *86*, 2593-2644, 1981.

Phipps Morgan, J., and Y. J. Chen, The genesis of oceanic crust: Magma injection, hydrothermal circulation, and crustal flow, *J. Geophys. Res.*, *98*, 6283-6298, 1993.

Pickering, J., and A. D. Johnston, The effects of variable mode on the melt productivity of fertile peridotitic assemblages (abstract), *Eos Trans. AGU*, *79*(45), Fall Meet. Suppl., F1004-F1005, 1998.

Quick, J. E., and R. P. Denlinger, Ductile deformation and the origin of layered gabbro in ophiolites, *J. Geophys. Res.*, *98*, 14,015-14,028, 1993.

Rabinowicz, M., A. Nicolas, and J.L. Vigneresse, A rolling mill effect in asthenosphere beneath oceanic spreading centers, *Earth Planet. Sci. Lett.*, *67*, 97–108, 1984.

Rabinowicz, M., G. Ceuleneer, and A. Nicolas, Melt segregation and flow in mantle diapirs below spreading centers: Evidence from the Oman ophiolite, *J. Geophys. Res.*, *92*, 3475-3486, 1987.

Schmeling, H., Numerical models on the influence of partial melt on elastic, anelastic and electric properties of rocks, part I, Elasticity and anelasticity, *Phys. Earth Planet. Inter.*, *41*, 34-57, 1985.

Shaw, P. R., and J. A. Orcutt, Waveform inversion of seismic refraction data and applications to young Pacific crust, *Geophys. J. R. Astron. Soc.*, *82*, 375-414, 1985.

Sinton, J. M., and R. S. Detrick, Mid-ocean ridge magma chambers, *J. Geophys. Res.*, *97*, 197-216, 1992.

Sleep, N. H., Tapping of melt by veins and dikes, *J. Geophys. Res.*, *93*, 10,255-10,272, 1988.

Solomon, S. C., and M. N. Toksöz, Lateral variation of attenuation of *P* and *S* waves beneath the United States, *Bull. Seismol. Soc. Am.*, *57*, 249-267, 1970.

Solomon, S. C., and D. R. Toomey, The structure of mid-ocean ridges, *Annu. Rev. Earth Planet. Sci.*, *20*, 329-364, 1992.

Stevenson, D. J., Spontaneous small-scale melt segregation in partial melts undergoing deformation, *Geophys. Res. Lett.*, *16*, 1067-1070, 1989.

Takanami, T., and G. Kitagawa, A new efficient procedure for the estimation of onset times of seismic waves, *J. Phys. Earth*, *36*, 267-290, 1988.

Thompson, R. N., Phase-equilibria constraints on the genesis and magmatic evolution of oceanic basalts, *Earth Sci. Rev.*, *24*, 161-210, 1987.

Thurber, C. H., Earthquake locations and three-dimensional crustal structure in the Coyote Lake area, central California, *J. Geophys. Res.*, *88*, 8226-8236, 1983.

Toomey, D. R., and G. R. Foulger, Application of tomographic inversion to local earthquake data from the Hengill-Grensdalur central volcano complex, Iceland, *J. Geophys. Res.*, *94*, 17,497-17,510, 1989.

Toomey, D. R., G. M. Purdy, S. C. Solomon, and W. S. D. Wilcock, The three-dimensional seismic velocity structure of the East Pacific Rise near latitude 9°30'N, *Nature*, *347*, 639-645, 1990.

Toomey, D. R., S. C. Solomon, and G. M. Purdy, Tomographic imaging of the shallow crustal structure of the East Pacific Rise at 9°30'N, *J. Geophys. Res.*, *99*, 24,135-24,157, 1994.

Vera, E. E., J. C. Mutter, P. Buhl, J. A. Orcutt, A. J. Harding, M. E. Kappus, R. S. Detrick, and T. M. Brocher, The structure of 0- to 0.2-m.y.-old oceanic crust at 9°N on the East Pacific Rise from expanded spread profiles, *J. Geophys. Res.*, *95*, 15,529-15,556, 1990.

Wang, X., J. R. Cochran, and G. A. Barth, Gravity anomalies, crustal thickness, and the pattern of mantle flow at the fast spreading East Pacific Rise, 9°-10°N: Evidence for three-dimensional upwelling, *J. Geophys. Res.*, *101*, 17,927-17,940, 1996.

Whitehead, J. A., H. J. B. Dick, and H. Schouten, A mechanism for magmatic accretion under spreading centres, *Nature*, *312*, 146-148, 1984.

Wilcock, W. S. D., and J. R. Delaney, Mid-ocean ridge sulfide deposits: Evidence for heat extraction from magma chambers or cracking fronts?, *Earth Planet. Sci. Lett.*, *145* 49-64, 1996.

Wilcock, W. S. D., S. C. Solomon, G. M. Purdy, and D. R. Toomey, The seismic attenuation structure of a fast-spreading mid-ocean ridge, *Science*, *258*, 1470-1474, 1992.

Wilcock, W. S. D., M. E. Dougherty, S. C. Solomon, G. M. Purdy, and D. R. Toomey, Seismic propagation across the East Pacific Rise: Finite difference experiments and implications for seismic tomography, *J. Geophys. Res.*, *98*, 19,913-19,932, 1993.

Wilcock, W. S. D., S. C. Solomon, G. M. Purdy, and D. R. Toomey, Seismic attenuation structure of the East Pacific Rise near 9°30'N, *J. Geophys. Res.*, *100*, 24,147-24,165, 1995.

R. Dunn, Department of Geological Sciences, 1846 Brown University, Providence, RI 02912-1846. (robert_allen_dunn@brown.edu)

S. C. Solomon, Department of Terrestrial Magnetism, Carnegie Institution of Washington, 5241 Broad Branch Road, N.W., Washington, DC 20015.

D. R. Toomey, Department of Geological Sciences, 1272 University of Oregon, Eugene, OR 97403-1272.

(Received July 27, 1999; revised March 2, 2000;
accepted June 9, 2000.)